JBC RESEARCH ARTICLE

Fission yeast Duf89 and Duf8901 are cobalt/nickel-dependent phosphatase–pyrophosphatases that act *via* a covalent aspartyl–phosphate intermediate

Received for publication, March 5, 2022, and in revised form, March 15, 2022 Published, Papers in Press, March 18, 2022,
https://doi.org/10.1016/j.jbc.2022.101851

Ana M. Sanchez[1,2], **Agata Jacewicz**[1], **and Stewart Shuman**[1,*]

From the [1]*Molecular Biology Program, Memorial Sloan Kettering Cancer Center, New York, New York, USA;* [2]*Gerstner Sloan Kettering Graduate School of Biomedical Sciences, New York, New York, USA*

Edited by Wolfgang Peti

Domain of Unknown Function 89 (DUF89) proteins are metal-dependent phosphohydrolases. Exemplary DUF89 enzymes differ in their metal and phosphosubstrate preferences. Here, we interrogated the activities and structures of two DUF89 paralogs from fission yeast—Duf89 and Duf8901. We find that Duf89 and Duf8901 are cobalt/nickel-dependent phosphohydrolases adept at hydrolyzing *p*-nitrophenylphosphate and PP_i. Crystal structures of metal-free Duf89 and Co^{2+}-bound Duf8901 disclosed two enzyme conformations that differed with respect to the position of a three-helix module, which is either oriented away from the active site in Duf89 or forms a lid over the active site in Duf8901. Lid closure results in a 16 Å movement of Duf8901 Asp195, vis-à-vis Asp199 in Duf89, that brings Asp195 into contact with an octahedrally coordinated cobalt. Reaction of Duf8901 with $BeCl_2$ and NaF in the presence of divalent cations Co^{2+}, Ni^{2+}, or Zn^{2+} generated covalent Duf8901-(Asp248)–beryllium trifluoride (BeF_3)•Co^{2+}, Duf8901-(Asp248)–BeF_3•Ni^{2+}, or Duf8901-(Asp248)–BeF_3•Zn^{2+} adducts, the structures of which suggest a two-step catalytic mechanism *via* formation and hydrolysis of an enzyme-(aspartyl)–phosphate intermediate. Alanine mutations of Duf8901 Asp248, Asn249, Lys401, Asp286, and Asp195 that interact with BeF_3•Co^{2+} squelched *p*-nitrophenylphosphatase activity. A 1.8 Å structure of a Duf8901-(Asp248)–AlF_4–OH_2•Co^{2+} transition-state mimetic suggests an associative mechanism in which Asp195 and Asp363 orient and activate the water nucleophile. Whereas deletion of the *duf89* gene elicited a phenotype in which expression of phosphate homeostasis gene *pho1* was derepressed, deleting *duf8901* did not, thereby hinting that the DUF89 paralogs have distinct functional repertoires *in vivo*.

Domain of Unknown Function 89 (DUF89) proteins comprise a large clade of homologous polypeptides found in taxa from all domains of life (1). Whereas a crystal structure of a DUF89 family member from *Arabidopsis* revealed a novel fold and a potential enzyme active site (2), the imputed DUF89 enzyme activity remained nebulous until Huang *et al.* (1) queried recombinant DUF89 family proteins from *Pyrococcus* (archaeon), *Arabidopsis* (plant), and *Saccharomyces* (budding yeast) for phosphohydrolase activities against a panel of 96 phosphosubstrates and found that DUF89s comprise a new clade of metal-dependent phosphatases. These DUF89s varied with respect to their metal cofactor preferences and substrate repertoires. The *Saccharomyces cerevisiae* DUF89 protein YMR027W was especially active in hydrolyzing fructose-1-phosphate and, with lower catalytic efficiency, fructose-6-phosphate (1). A structure obtained after soaking YMR027W crystals in fructose-6-phosphate showed the sugar phosphate moiety positioned adjacent to a single magnesium ion in the active site (1). It was suggested that DUF89 family members may function to limit potentially harmful buildups of normal or damaged phosphometabolites. Initial studies had assigned an enzymatic function to the human DUF89-family protein C6orf211 as an AdoMet-dependent protein glutamate methyltransferase (3). Dennis *et al.* (4) subsequently clarified that human C6orf211/DUF89 is a cobalt-dependent phosphomonoesterase devoid of methyltransferase activity. Budding yeast YMR027W and human C6orf211 belong to the so-called subfamily III of DUF89 proteins, which are of similar size (~380–480 amino acids) and have a characteristic RTxK motif situated ~40 to 50 amino acids from their C termini (1).

The fission yeast *Schizosaccharomyces pombe* genome encodes two subfamily III DUF89 paralogs: SPCC1393.13 (referred to henceforth as Duf89) and SPAC806.04c (henceforth Duf8901). Alignment of the 442-amino acid Duf89 and 438-amino acid Duf8901 proteins highlights 312 positions of side-chain identity/similarity. Our interest in Duf89 was prompted by the finding by Henry *et al.* (5) that deletion of the fission yeast SPCC1393.13 gene results in elevated expression of the phosphate homeostasis gene *pho1*. Whereas the significance of this finding was unclear at the time, it is now known that *pho1* is actively repressed during growth in phosphate-rich medium by the transcription in *cis* of a long noncoding (lnc) RNA from the 5′ flanking gene *prt*(*nc-pho1*) (reviewed in Ref. (6)). lncRNA 3′ processing/termination is a key control point in *pho1* mRNA repression. Tandem lncRNA–mRNA transcriptional interference can be tuned by increasing or decreasing the frequency with which RNA polymerase II terminates lncRNA transcription prior to encounter with the mRNA promoter (6). Genetic manipulations that enhance or

* For correspondence: Stewart Shuman, shumans@mskcc.org.

diminish "precocious" termination of lncRNA transcription result in derepression or hyper-repression of *pho1* mRNA expression in phosphate-replete cells. In particular, lncRNA-mediated transcription interference is sensitive to mutation of several phosphohydrolase enzymes that act on phosphoproteins or inositol pyrophosphates (IPPs) (7, 8).

To establish a framework for understanding the physiology of DUF89 proteins in fission yeast, and to further illuminate the mechanism of the DUF89 enzyme family, we produced and purified recombinant Duf89 and Duf8901 proteins and interrogated their biochemical properties and atomic structures. We find that Duf89 and Duf8901 are cobalt/nickel-dependent phosphohydrolases with vigorous activity against *p*-nitrophenylphosphate (a phosphomonoester). Duf89 and Duf8901 are also able to hydrolyze PP_i (a phosphoanhydride) in the presence of cobalt or nickel. Human DUF89 also has cobalt/nickel-dependent pyrophosphatase activity. We present crystal structures of fission yeast Duf89 and Duf8901 that highlight two enzyme conformations that differ with respect to the position of a three-helix module, which is either oriented away from the active-site pocket in Duf89•PO_4 (open state) or forms a lid over the active-site pocket in Duf8901•Co^{2+} (closed state). We demonstrate that Duf8901 reacts with $BeCl_2$ and NaF in the presence of divalent cations Co^{2+}, Ni^{2+}, or Zn^{2+} to form covalent Duf8901-(Asp248)–BeF_3•Co^{2+}, Duf8901-(Asp248)–BeF_3•Ni^{2+}, or Duf8901-(Asp248)–BeF_3•Zn^{2+} adducts, the structures of which illuminate a two-step catalytic mechanism *via* formation and hydrolysis of an aspartyl–phosphate intermediate. A 1.8 Å structure of a Duf8901-(Asp248)–aluminum fluoride (AlF_4)–OH_2•Co^{2+} transition-state mimetic suggests an associative mechanism of phosphoenzyme hydrolysis in which Asp195 and Asp363 orient and activate the water nucleophile. Whereas deleting the *duf89* gene derepressed fission yeast Pho1 expression, deleting *duf8901* did not, suggesting that the two DUF89 phosphatase paralogs have distinct substrate preferences *in vivo*.

Results

Recombinant S. pombe *Duf89 is a cobalt/nickel-dependent phosphohydrolase*

We produced recombinant wildtype Duf89 in *Escherichia coli* as a His_{10}Smt3 fusion and isolated it from a soluble bacterial extract by Ni-affinity chromatography. The tag was removed by treatment with the Smt3 protease Ulp1, and Duf89 was recovered free of His_{10}Smt3 after a second round of Ni-affinity chromatography (Fig. 1*A*). To interrogate Duf89 enzymatic function, we tested its activity with the generic phosphomonoesterase substrate *p*-nitrophenylphosphate. Hydrolysis of *p*-nitrophenylphosphate liberates *p*-nitrophenol, which is quantified by its absorbance at 410 nm. We found that Duf89 readily converted 10 mM *p*-nitrophenylphosphate into *p*-nitrophenol during a 30 min reaction at 37 °C in the presence of 0.5 mM nickel or cobalt (Fig. 1*C*). Zinc, manganese, magnesium, and cadmium were progressively less effective than nickel or cobalt in supporting phosphomonoesterase activity; copper and calcium were inactive (Fig. 1*C*). In parallel, we tested Duf89 for phosphodiesterase activity with the generic substrate bis-*p*-nitrophenylphosphate. No release of *p*-nitrophenol was detected in reactions containing 0.5 mM nickel, cobalt, zinc, magnesium, manganese, cadmium, calcium, or copper. Subsequent characterization of the *p*-nitrophenylphosphatase activity of Duf89 was performed using 0.5 mM cobalt as the metal cofactor.

Duf89 phosphatase was optimal at pH 6.0 to 6.5; activity declined gradually as the pH was increased to 9.5 and more steeply when pH was lowered to 4.5 (Fig. 1*D*). The extent of *p*-nitrophenylphosphate hydrolysis during a 30 min reaction increased steadily with input Duf89 up to 20 pmol and continued to increase with a shallower slope in the range of 20 to 120 pmol (Fig. 1*E*). No hydrolysis of *p*-nitrophenylphosphate was detectable during a 30 min reaction with cobalt in the absence of Duf89 (Fig. 1*E*). From the slope of the Duf89 titration curve in the steeper initial phase, we calculated a specific activity of 8.36 nmol of *p*-nitrophenol formed per pmol of Duf89, which translates into an estimated turnover number of 4.6 s^{-1}. Duf89 activity during a 5 min reaction under steady-state conditions (<6% of substrate consumed) displayed a hyperbolic dependence on *p*-nitrophenylphosphate concentration (Fig. 1*F*). Fitting the data to the Michaelis–Menten equation yielded K_m and k_{cat} values of 11.0 ± 2.0 mM and 9.72 ± 1.13 s^{-1}, respectively (R squared = 0.9811). Gel filtration of Duf89 through a Superdex-200 column showed that the phosphatase activity profile coincided with that of the Duf89 polypeptide (Fig. S1); the Duf89 peak elution volume was consistent with it being a monomer in solution.

Effect of mutations of predicted Duf89 metal-binding residues

A primary structure alignment of *S. pombe* Duf89 (442 amino acids) and *S. cerevisiae* YMR027W (470 amino acids) highlighted 237 positions of amino acid side-chain identity/similarity (Fig. S2*A*). Fig. S2*B* shows a stereo view of the active site of YMR027W, occupied by two phosphate anions and a manganese ion (1; Protein Data Bank [PDB] ID: 5F13). The amino acids of YMR027W that engage the phosphates and the metal cofactor are conserved in *S. pombe* Duf89 as Asp252, Asn253, Asp290, Arg371, and Lys405 (shaded in *cyan* in Fig. S2*A*). To affirm that the observed phosphatase activity inhered to the recombinant Duf89 protein, we produced and purified two mutated versions in which the predicted metal-binding active-site amino acids Asp252 and Asp290 were replaced singly by alanine (Fig. 1*A*). Parallel assays of the wildtype and mutant Duf89s showed that activity was abolished by the D252A and D290A mutations (Fig. 1*B*).

Duf89 activity is inhibited by phosphate

Budding yeast YMR027W crystals with two phosphate ions in the active site were grown by Huang *et al.* (1) using a precipitant/reservoir solution containing 0.5 M phosphate. The presence of two phosphates in a subfamily III DUF89 protein raises the following questions regarding fission yeast Duf89: (i) Does it act on polyphosphorylated substrates? (ii) Is

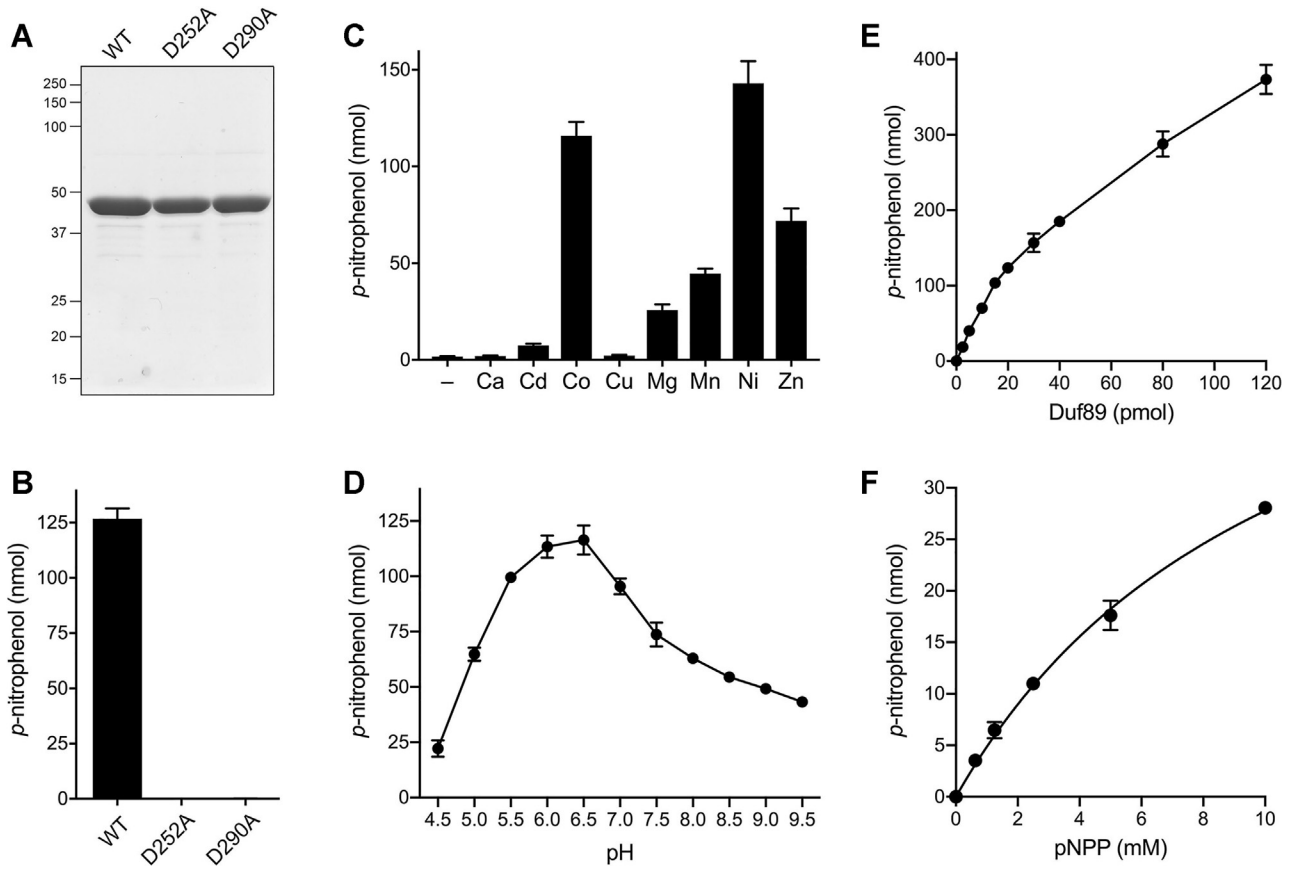

Figure 1. Duf89 phosphatase activity with *p*-nitrophenylphosphate. *A*, aliquots (10 μg) of the indicated wildtype or mutant Duf89 preparations analyzed by SDS-PAGE. The Coomassie blue–stained gel is shown. The positions and sizes (kilodalton) of marker polypeptides are indicated on the *left*. *B*, phosphatase reaction mixtures (50 μl) containing 50 mM Tris-acetate (pH 6.5), 50 mM NaCl, 10 mM (500 nmol) *p*-nitrophenylphosphate, 0.5 mM $CoCl_2$, and 0.4 μM (20 pmol) of the wildtype or mutant Duf89 preparations were incubated at 37 °C for 30 min. The extents of *p*-nitrophenol production are plotted. *C*, metal cofactor specificity. Reaction mixtures (50 μl) containing 50 mM Tris-acetate (pH 6.5), 50 mM NaCl, 10 mM (500 nmol) *p*-nitrophenylphosphate, either no added metal (–) or 0.5 mM of the divalent cation specified on the *x*-axis, and 0.4 μM (20 pmol) Duf89 were incubated at 37 °C for 30 min. The extents of *p*-nitrophenol production are plotted. *D*, pH profile. Reaction mixtures (50 μl) containing 50 mM buffer (either Tris-acetate pH 4.5, 5.0, 5.5, 6.0, 6.5; or Tris–HCl pH 7.0, 7.5, 8.0, 8.5, 9.0, 9.5), 50 mM NaCl, 10 mM (500 nmol) *p*-nitrophenylphosphate, 0.5 mM $CoCl_2$, and 0.4 μM (20 pmol) Duf89 were incubated at 37 °C for 30 min. The extents of *p*-nitrophenol production are plotted. *E*, Duf89 titration. Reaction mixtures constituted as in *B* and containing increasing amounts of Duf89 as specified on the *x*-axis were incubated at 37 °C for 30 min. *p*-Nitrophenol production is plotted as a function of input Duf89. *F*, steady-state kinetic parameters. Reaction mixtures (50 μl) containing 50 mM Tris-acetate (pH 6.5), 50 mM NaCl, 0.5 mM $CoCl_2$, 0.4 μM (20 pmol) Duf89, and increasing concentrations of *p*-nitrophenylphosphate as specified on the *x*-axis were incubated at 37 °C for 5 min. *p*-Nitrophenol production is plotted as a function of substrate concentration, and the data were fit to the Michaelis–Menten equation in Prism. All data plotted in *B–F* are the averages of three independent experiments ± SEM. Duf89, Domain of Unknown Function 89.

Duf89 inhibited by free phosphate? To address the latter issue, we supplemented the standard reaction mixtures containing 10 mM *p*-nitrophenylphosphate with increasing concentrations of sodium phosphate (pH 6.5) up to 100 mM. Two sets of control reactions were supplemented with the equivalent concentrations of sodium chloride or sodium sulfate. Phosphate elicited a concentration-dependent inhibition of Duf89 phosphatase activity, by 47% at 5 mM phosphate compared with the no phosphate control, and by 69%, 82%, 91%, and 96% at 10, 20, 50, and 100 mM phosphate, respectively (Fig. 2). These results suggest that orthophosphate (a reaction product) binds to the active site as well as, or better than, the *p*-nitrophenylphosphate substrate. By contrast, sulfate and chloride had relatively little impact, even up to 100 mM, at which point, activity was diminished by only 29% (chloride) or 30% (sulfate) compared with the unsupplemented control (Fig. 2).

Duf89 hydrolyzes inorganic pyrophosphate (PPi)

Duf89 (0.1 μM) was reacted for 60 min with 1 mM PP_i in the presence of a panel of divalent cations at a concentration of 0.5 mM. The formation of P_i product was determined *via* colorimetric assay using the Malachite Green reagent. Duf89 catalyzed optimal hydrolysis of PP_i to P_i in the presence of cobalt or nickel (870–1150 pmol of P_i formed or 435–575 pmol of PP_i hydrolyzed, per pmol of Duf89, which translates into lower bound estimates of turnover numbers of 7.3–9.8 min^{-1} with cobalt and nickel, respectively) (Fig. 3*B*). No pyrophosphatase activity was detected in the absence of added divalent cation. Copper, zinc, magnesium, and manganese were progressively less effective than nickel or cobalt in supporting pyrophosphatase activity; calcium and cadmium were inactive (Fig. 3*B*). Hydrolysis of 1 mM PP_i was optimal at 0.5 mM cobalt or 0.5 to 1 mM nickel (Fig. 3*C*). Pyrophosphatase activity was abolished by Duf89 mutations D252A and D290A (Fig. 3*A*).

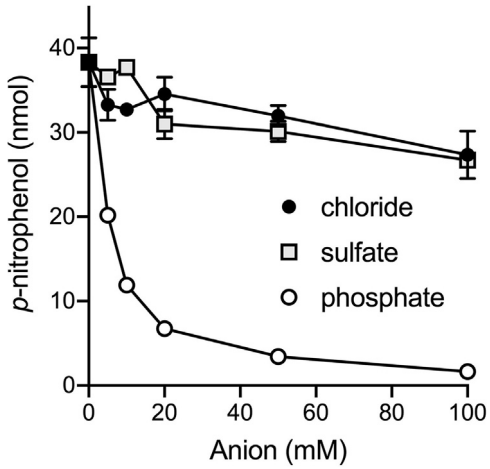

Figure 2. Duf89 activity is inhibited by phosphate. Reaction mixtures (50 μl) containing 50 mM Tris-acetate (pH 6.5), 50 mM NaCl, 10 mM (500 nmol) *p*-nitrophenylphosphate, 0.5 mM $CoCl_2$, and 0.4 μM (20 pmol) Duf89 were supplemented with sodium chloride, sodium sulfate, or sodium phosphate (pH 6.5) at the concentrations specified on the *x*-axis. The reaction mixtures were incubated at 37 °C for 5 min. The extents of *p*-nitrophenol production are plotted as a function of added anion concentration. Each datum is the average of three separate titration experiments ± SEM. Duf89, Domain of Unknown Function 89.

Pyrophosphatase activity displayed a hyperbolic dependence on PP_i concentration (Fig. 3*D*). Fitting the data to the Michaelis–Menten equation yielded a K_m value of 1.15 ± 0.16 mM PP_i and an apparent k_{cat} of 31.9 ± 1.7 min^{-1} (*R* squared = 0.966) with respect to moles of PP_i consumed per enzyme. That the apparent K_m of Duf89 for PP_i was 10-fold lower than its K_m for the generic phosphomonoester *p*-nitrophenylphosphate hints that a pyrophosphorylated metabolite might be a relevant substrate for Duf89 in fission yeast. We suspect that the lower turnover number for the Duf89 pyrophosphatase *versus* *p*-nitrophenylphosphatase reactions reflects slower dissociation of the phosphate leaving group of pyrophosphate from the active site *versus* more rapid dissociation of the *p*-nitrophenol leaving group of *p*-nitrophenylphosphate.

Fission yeast Duf8901 is a phosphatase/pyrophosphatase paralog of Duf89

We produced and purified recombinant Duf8901 protein (Fig. 4*A*). Duf8901 hydrolyzed 10 mM *p*-nitrophenylphosphate to *p*-nitrophenol in the presence of 0.5 mM nickel or cobalt (Fig. 4*B*). Zinc, manganese, magnesium, and cadmium were progressively less effective than nickel or cobalt in supporting phosphomonoesterase activity; copper and calcium were inactive (Fig. 4*B*). The extent of *p*-nitrophenol formation in a 30 min reaction with 0.5 mM cobalt was proportional to input Duf8901 (Fig. 4*C*). No hydrolysis of *p*-nitrophenylphosphate was detectable during a 30 min reaction with cobalt in the absence of Duf8901 (Fig. 4*C*). We calculated a specific activity of 2.3 nmol of *p*-nitrophenol formed per pmol of Duf8901, which translates into an estimated turnover number of 1.28 s^{-1}. Duf8901 activity during a 5 min reaction under steady-state conditions (<6% of substrate consumed) displayed a hyperbolic dependence on *p*-nitrophenylphosphate concentration (Fig. 4*D*). Fitting the data to the Michaelis–Menten equation yielded K_m and k_{cat} values of 6.48 ± 1.2 mM and 2.89 ± 0.29 s^{-1}, respectively (R squared = 0.969). Duf8901 hydrolysis of 10 mM *p*-nitrophenylphosphate was inhibited in a concentration-dependent manner by phosphate, with an IC_{50} of ∼10 mM phosphate and IC_{90} of ∼75 mM phosphate (Fig. 4*E*). Sulfate and chloride had comparatively little effect, even up to 100 mM, at which point Duf8901 activity was diminished by 20% (chloride) or 47% (sulfate) compared with the unsupplemented control (Fig. 4*E*).

Duf8901 also catalyzed cobalt-dependent and nickel-dependent hydrolysis of PP_i (Fig. 4*G*). Zinc and magnesium were less effective as metal cofactors; manganese, calcium, cadmium, and copper were ineffective. The inorganic pyrophosphatase specific activity of Duf8901 in the presence of cobalt, calculated from the slope of the titration curve (Fig. 4*F*), was 58.3 pmol of phosphate released (*i.e.*, 29.2 pmol of PP_i hydrolyzed) per pmol of Duf8901, which translates into an estimated turnover number of 0.49 min^{-1}. Thus, whereas the *p*-nitrophenylphosphatase specific activity of Duf8901 was 28% of that observed for Duf89 assayed under the same conditions, the inorganic pyrophosphatase activity of Duf8901 was 7% of that observed for Duf89 assayed under the same conditions. We surmise that Duf89 is a more vigorous pyrophosphatase enzyme than is its Duf8901 paralog.

Human DUF89 is a cobalt/nickel-dependent pyrophosphatase

The human C6orf211 gene encodes a 441-amino acid polypeptide that shares 201 positions of side-chain identity/similarity with fission yeast Duf89. In light of our findings here that *S. pombe* DUF89s have pyrophosphatase activity, we queried if human DUF89 protein is also competent for pyrophosphate hydrolysis. We produced recombinant human DUF89 in *E. coli* and purified it *via* sequential Ni-affinity chromatography, His_{10}Smt3 tag cleavage, and His_{10}Smt3 tag-depletion steps (Fig. S3*A*). We first affirmed that human DUF89 displayed metal-dependent phosphomonoesterase activity against *p*-nitrophenylphosphate, with cobalt and nickel as the preferred cofactors (Fig. S3*B*). Human DUF89 hydrolyzed 74.5 nmol of *p*-nitrophenylphosphate per 20 pmol of enzyme during a 30 min reaction in the presence of cobalt, which translates into an estimated turnover number of 2.1 s^{-1} (*i.e.*, ∼45% as active as fission yeast Duf89 assayed under the same conditions). A distinctive feature of human DUF89 *versus* fission yeast Duf89 is that zinc is not an effective cofactor for *p*-nitrophenylphosphate hydrolysis by the human enzyme (compare Figs. S3*B* and 1*C*). Here, we found that human DUF89 also hydrolyzed PP_i, with optimal activity in the presence of cobalt or nickel (Fig. S3*C*). Human DUF89 hydrolyzed 2540 pmol of pyrophosphate per 10 pmol of enzyme during a 60 min reaction with cobalt, which translates into an estimated turnover number of 4.2 min^{-1} (*i.e.*, ∼58% as active as fission yeast Duf89 assayed under the same conditions).

Crystal structure of fission yeast Duf89

We grew crystals from a premixed solution of Duf89 with 5 mM cobalt and 10 mM PP_i. The Duf89 crystals diffracted

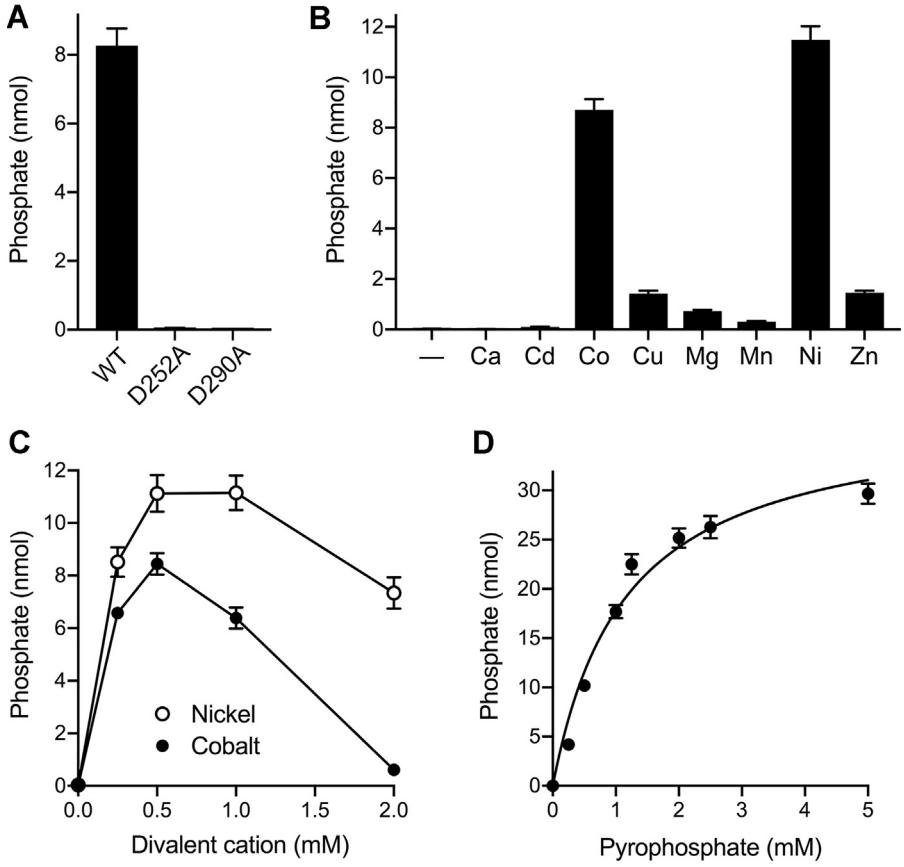

Figure 3. Duf89 hydrolyzes PP_i. *A*, pyrophosphatase reaction mixtures (100 μl) containing 50 mM Tris-acetate (pH 6.5), 25 mM NaCl, 1 mM (100 nmol) PP_i, 0.5 mM $CoCl_2$, and 0.1 μM (10 pmol) of wildtype or mutant Duf89 preparations were incubated at 37 °C for 60 min. The extents of phosphate production are plotted. *B*, metal cofactor specificity. Reaction mixtures (100 μl) containing 50 mM Tris-acetate (pH 6.5), 25 mM NaCl, 1 mM (100 nmol) PP_i, either no added metal (–) or 0.5 mM of the divalent cation specified on the *x*-axis, and 0.1 μM (10 pmol) Duf89 were incubated at 37 °C for 60 min. The extents of phosphate production are plotted. *C*, metal titration. Reaction mixtures (100 μl) containing 50 mM Tris-acetate (pH 6.5), 25 mM NaCl, 1 mM (100 nmol) PP_i, 0.1 μM (10 pmol) Duf89, and varying concentrations $CoCl_2$ or $NiCl_2$ as specified on the *x*-axis were incubated at 37 °C for 60 min. Phosphate production is plotted as a function of divalent cation concentration. *D*, steady-state kinetic parameters. Reaction mixtures (100 μl) containing 50 mM Tris-acetate (pH 6.5), 25 mM NaCl, 0.5 mM $CoCl_2$, 0.2 μM (20 pmol) Duf89, and increasing concentrations of PP_i as specified on the *x*-axis were incubated at 37 °C for 30 min. Phosphate production is plotted as a function of substrate concentration, and the data were fit to the Michaelis–Menten equation in Prism. The data plotted in *A–D* are the averages of three independent experiments ± SEM. Duf89, Domain of Unknown Function 89.

X-rays to a resolution of 2.0 Å, were in space group C2, and contained one Duf89 protomer in the asymmetric unit (ASU). The structure was solved as described under the Experimental procedures section and summarized in Table S1. The refined model (R/R_{free} = 16.0/20.0) comprised a continuous polypeptide from Leu3 to Asp442. A stereo view of the Duf89 tertiary structure is shown in Figure 5*A*. It is composed of seven β-strands, 21 α helices, and five 3_{10} helices, which are displayed over the amino acid sequence in Figure 6. The fold consists of a β-sheet (with topology β1↓•β7↓•β6↑•β5↑•β2↑•β3↑•β4↑) flanked on both sides by helices. The fold is stabilized by a multitude of salt bridges (Arg122-Asp92, Arg131-Glu65, Arg344-Glu99, Arg371-Asp376, Arg243-Glu272, Arg246-Asp355, Arg246-Asp248, Arg331-Asp355, Arg402-Asp367, Arg149-Asp145, Arg161-Glu187, Arg161-Glu168, Lys144-Asp295, Lys144-Asp138, Lys152-Glu156, Lys365-Asp261, Lys365-Glu257, and Lys225-Glu222) and by an Arg371-Trp113 cation–π stack. A surface electrostatic model (Fig. 5*B*) highlights the presence of single phosphate anion within a deep active-site pocket that is exposed to solvent. Neither metal nor pyrophosphate (the input ligands) were evident, suggesting that the pyrophosphate substrate had been hydrolyzed in the presence of cobalt and that the metal cofactor and one of the two phosphate products had dissociated from the enzyme, abetted perhaps by chelation of the metal by the 0.1 M citrate present in the precipitant solution used for crystal growth. The phosphate is coordinated by Asp252-Oδ, Glu257-Oε, Thr403-Oγ, and Leu193-O (Fig. 5*C*). These atypical contacts suggest that the Duf89-bound phosphate is in the form of a H_2PO_4 monoanion, thereby allowing for hydrogen bonding to the carboxylate and carbonyl moieties. This is plausible insofar as the pH of the crystallization solution was 5.0.

A Dali search (9) of the PDB recovered the human and *S. cerevisiae* DUF89 proteins (members of subfamily III) as the top "hits" with Z scores of ≥48, amino acid identity of 33 to 37%, and rmsds of 1.7 to 1.9 Å at ≥400 Cα positions (Table S2). Lesser structure homology was apparent to DUF89 proteins from *Arabidopsis* (subfamily II; Z score of 22) and the archaeal taxa *Pyrococcus* and *Archaeoglobus* (subfamily I; Z scores of 18–19) (Table S2). Superimpositions of the crystal structures highlighted the fact that the protein segment corresponding to

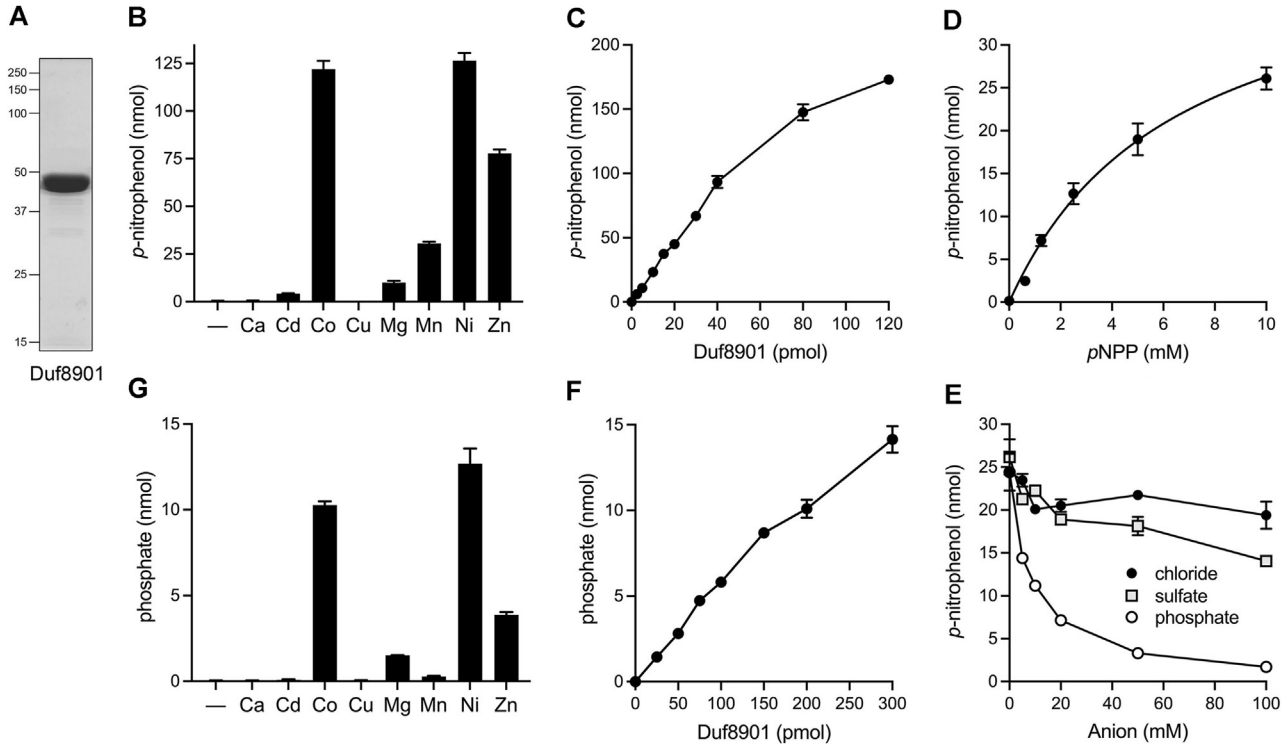

Figure 4. Phosphatase and pyrophosphatase activities of fission yeast Duf8901. *A*, an aliquot (10 μg) of purified recombinant Duf8901 was analyzed by SDS-PAGE. The Coomassie blue–stained gel is shown. The positions and sizes (kilodalton) of marker polypeptides are indicated on the *left*. *B*, metal cofactor specificity for hydrolysis of *p*-nitrophenylphosphate. Reaction mixtures (50 μl) containing 50 mM Tris-acetate (pH 6.5), 50 mM NaCl, 10 mM (500 nmol) *p*-nitrophenylphosphate, either no added metal (–) or 0.5 mM of the divalent cation specified on the *x*-axis, and 1 μM (50 pmol) Duf8901 were incubated at 37 °C for 30 min. The extents of *p*-nitrophenol production are plotted. *C*, Duf8901 titration. Reaction mixtures (50 μl) containing 50 mM Tris-acetate (pH 6.5), 50 mM NaCl, 10 mM (500 nmol) *p*-nitrophenylphosphate, 0.5 mM $CoCl_2$, and increasing amounts of Duf89 as specified on the *x*-axis were incubated at 37 °C for 30 min. *p*-Nitrophenol production is plotted as a function of input Duf8901. *D*, steady-state kinetic parameters. Reaction mixtures (50 μl) containing 50 mM Tris-acetate (pH 6.5), 50 mM NaCl, 0.5 mM $CoCl_2$, 1 μM (50 pmol) Duf8901, and increasing concentrations of *p*-nitrophenylphosphate as specified on the *x*-axis were incubated at 37 °C for 5 min. *p*-Nitrophenol production is plotted as a function of substrate concentration, and the data were fit to the Michaelis–Menten equation in Prism. *E*, inhibition by phosphate. Reaction mixtures (50 μl) containing 50 mM Tris-acetate (pH 6.5), 50 mM NaCl, 10 mM (500 nmol) *p*-nitrophenylphosphate, 0.5 mM $CoCl_2$, and 1 μM (50 pmol) Duf8901 were supplemented with sodium chloride, sodium sulfate, or sodium phosphate (pH 6.5) at the concentrations specified on the *x*-axis. The reaction mixtures were incubated at 37 °C for 5 min. The extents of *p*-nitrophenol production are plotted as a function of added anion concentration. *F*, hydrolysis of PP_i. Reaction mixtures (100 μl) containing 50 mM Tris-acetate (pH 6.5), 25 mM NaCl, 1 mM (100 nmol) PP_i, 0.5 mM $CoCl_2$, and increasing amounts of Duf8901 as specified on the *x*-axis were incubated at 37 °C for 60 min. Phosphate production is plotted as a function of input Duf8901. *G*, metal cofactor specificity for hydrolysis of PP_i. Reaction mixtures (100 μl) containing 50 mM Tris-acetate (pH 6.5), 25 mM NaCl, 1 mM (100 nmol) PP_i, either no added metal (–) or 0.5 mM of the divalent cation specified on the *x*-axis, and 1 μM (100 pmol) Duf8901 were incubated at 37 °C for 60 min. The extents of phosphate production are plotted. The data in *B*–*G* are the averages of three independent experiments ± SEM. Duf89, Domain of Unknown Function 89; Duf8901, Domain of Unknown Function 8901.

fission yeast Duf89 amino acids Gly195 to Ala219—which includes the α10, α11, and α12 helices—is disordered in the human DUF89 structure. The segment corresponding to fission yeast Duf89 amino acids Asn196 to Gln212 is also disordered in the budding yeast DUF89 structure.

Structure of Duf8901

Crystals of Duf8901 preincubated with 5 mM $CoCl_2$ were grown by vapor diffusion against precipitant solution containing 1.8 M sodium/potassium phosphate. The crystals diffracted X-rays to a resolution of 1.9 Å, were in space group $P22_12_1$, and contained two Duf8901 protomers in the ASU. The B protomer comprised a continuous polypeptide from Met1 to Ala438. The A protomer was punctuated by a disordered six-amino acid surface loop (from Ile168 to Asp173). The Duf8901 secondary structure elements are displayed under the amino acid sequence in Figure 6. The primary, secondary, and tertiary structures of Duf8901 and Duf89 were highly homologous; pairwise alignment of the Duf8901 B protomer to Duf89 in Dali yielded a Z score of 53.3 and an rmsd of 1.5 Å at ≥420 Cα positions. 27 of 31 of the basic and acidic side chains that form fold-stabilizing salt bridges in the Duf89 structure are conserved in Duf8901. Figure 7*A* shows a stereo view of the Duf8901 fold (depicted as a cartoon model with *cyan helices* and *magenta β-strands*) superimposed on that of Duf89 (rendered as a *green ribbon trace*). Duf8901 contains a single cobalt ion (*magenta sphere*) and corresponding anomalous difference peak (*green mesh* contoured at 3σ) in its active site (Fig. 7*B*). The metal ion is coordinated by Asp248-Oδ1, Asp286-Oδ1, Asn249-Oδ, Asp195-Oδ1 and Asp195-Oδ2, and Phe283-O (Fig. 7*B*). Duf8901 Asp248, Asp286, and Asn249 are conserved amino acids, the counterparts of which coordinate a manganese ion in the budding yeast DUF89 structure and a magnesium ion in the human DUF89 structure.

The proximity of Asp195 to the metal cofactor is a distinctive feature of the Duf8901•Co^{2+} complex, insofar as the corresponding conserved aspartates in budding yeast DUF89 (Asp195) and human DUF89 (Asp195) are located within their

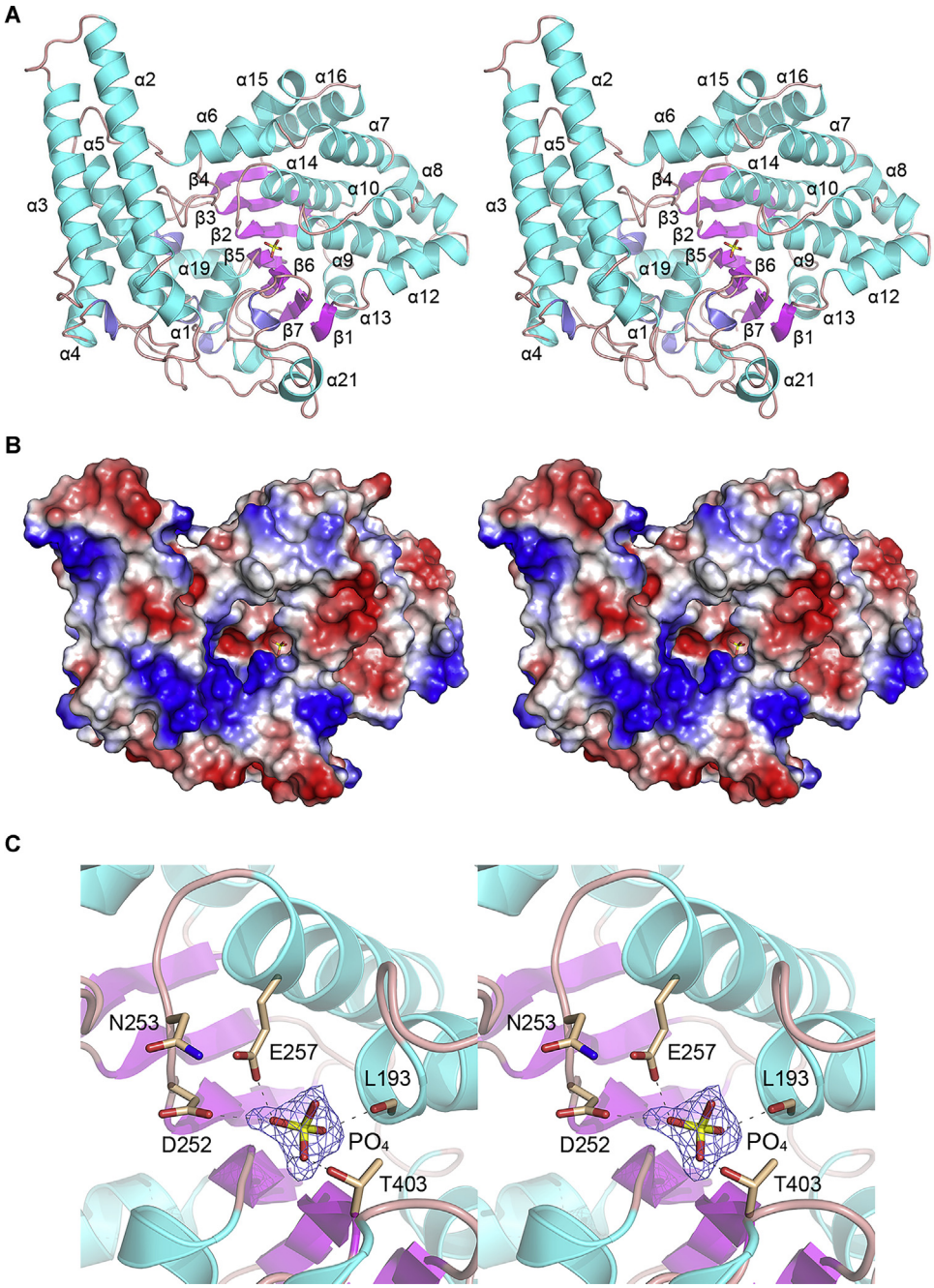

Figure 5. Structure of fission yeast Duf89. *A*, stereo view of the tertiary structure of Duf89, depicted as a *cartoon model* with *magenta β-strands*, *cyan α-helices*, and *blue 3_{10} helices*. The secondary structure elements of Duf89 are labeled according to their order in the primary structure, as shown in Figure 6. A phosphate ion adjacent to β5 is rendered as a *stick model*. *B*, surface electrostatic model of Duf89 generated in Pymol, looking down into the active-site pocket, in which a phosphate ion (*stick model*) is bound. *C*, stereo view of the Duf89 active site with selected amino acids depicted as *stick models* with *beige carbons*. Enzymic contacts to the phosphate are indicated by *dashed lines*. Omit density (F_o–F_c) for the phosphate is depicted as *blue mesh* contoured at 3σ. Duf89, Domain of Unknown Function 89.

respective disordered segments (embracing helices 10, 11, and 12 of the fission yeast proteins) that were mentioned in the preceding section. The counterpart of the helix-10,11 segment (containing Asp166) is disordered in the structure of an *Arabidopsis* DUF89•Mg^{2+} complex (PDB ID: 2Q40).

The superposition of Duf8901 and Duf89 in Figure 7*A* provides new insight by highlighting the mobility of the helix-10,11,12 module, which is depicted as a *yellow cartoon model* for Duf8901 and a *green cartoon model* for Duf89 and demarcated by *arrows*. The α10,11,12 module in Duf89 is reflected away from the active-site pocket and packs against helices α7, α8, and α9 (Figs. 5*A* and 7*A*). By contrast, in Duf8901, the module has flipped over the active-site pocket, serving as a "lid" that closes off the active site (Fig. 7*A*). The lid closure entails a 16 Å movement of the Duf8901 Asp195-Cα vis-à-vis the corresponding Asp199-Cα in Duf89 (Fig. 7*A*), thereby bringing Asp195 into the orbit of the active-site metal ion. We envision that interaction of the conserved lid aspartate

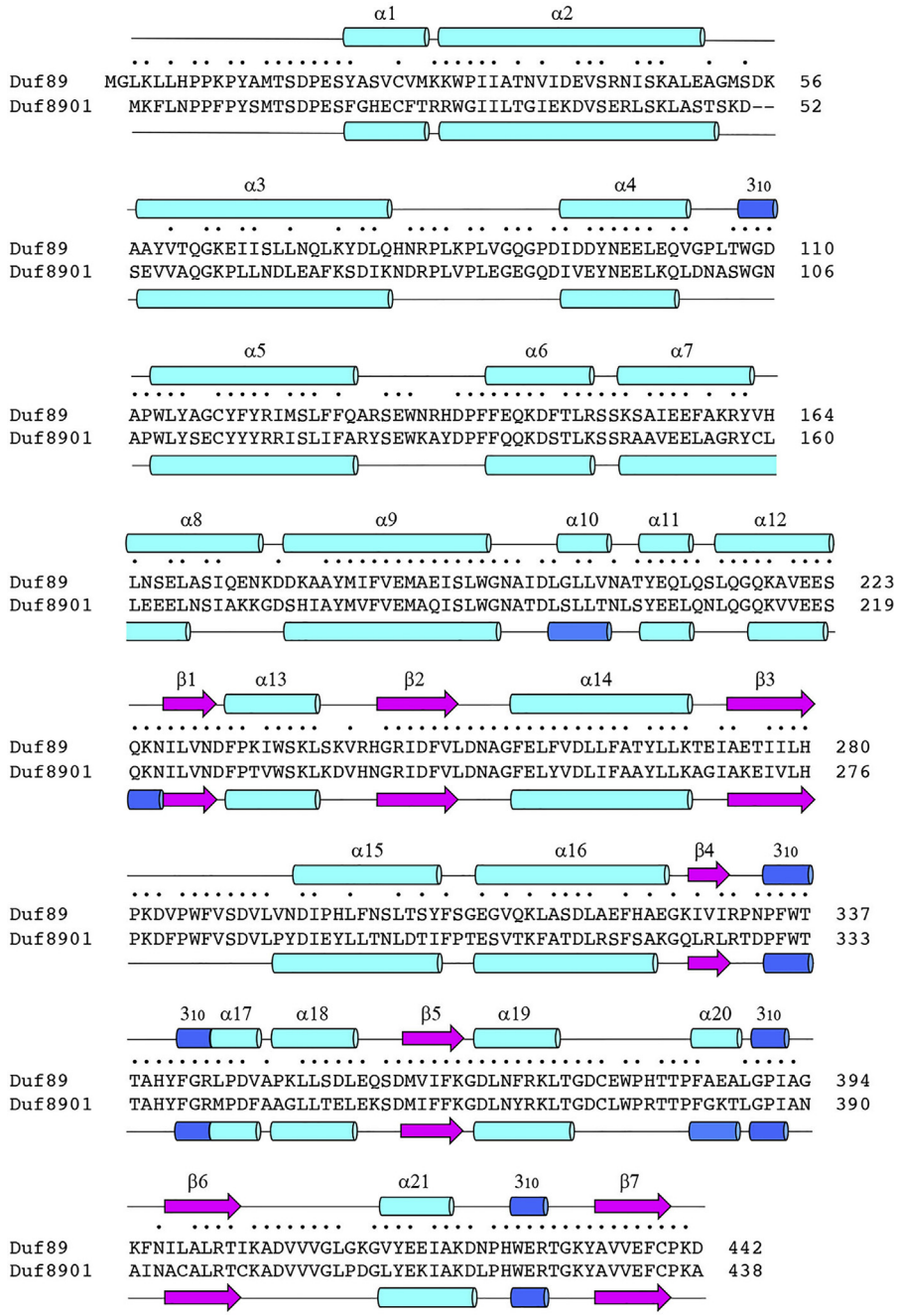

Figure 6. Primary and secondary structure homology of Duf89 and Duf8901. The amino acid sequences of Duf89 and Duf8901 are aligned. Positions of amino acid side-chain identity/similarity are denoted by *dots* above the Duf89 sequence. The secondary structure elements of Duf89 and Duf8901 are displayed above and below their respective primary structures, with β-strands depicted as *magenta arrows*, α-helices as *cyan cylinders*, and 3_{10} helices as *blue cylinders*. The secondary structure elements of Duf89 are labeled as in Figure 5*A*. Duf89, Domain of Unknown Function 89; Duf8901, Domain of Unknown Function 8901.

with the active-site metal either triggers lid closure or else stabilizes the closed conformation, which could explain why there is no phosphate anion seen in the Duf8901•Co^{2+} complex, notwithstanding the presence of 1.8 M phosphate in the crystallization solution.

Structure of a BeF_3 mimetic of a Duf8901 aspartyl–phosphate intermediate

In the budding yeast DUF89 crystal structure in complex with phosphates and manganese (1), the octahedral metal coordination complex is filled by two aspartates and an asparagine, a phosphate oxygen (from the putative scissile phosphate), and two waters (Fig. S2*B*). It is noteworthy that one of the metal-binding aspartates (Asp254, equivalent to Asp252 in *S. pombe* Duf89 and Asp248 in Duf8901) is positioned so that its Oδ2 atom is 3.2 Å from the phosphorus atom of the scissile phosphate, raising the prospect that catalysis of DUF89 enzymes might proceed *via* nucleophilic attack of this aspartate on the scissile phosphate to form a covalent enzyme acyl–phosphate intermediate (1). This mechanism of covalent

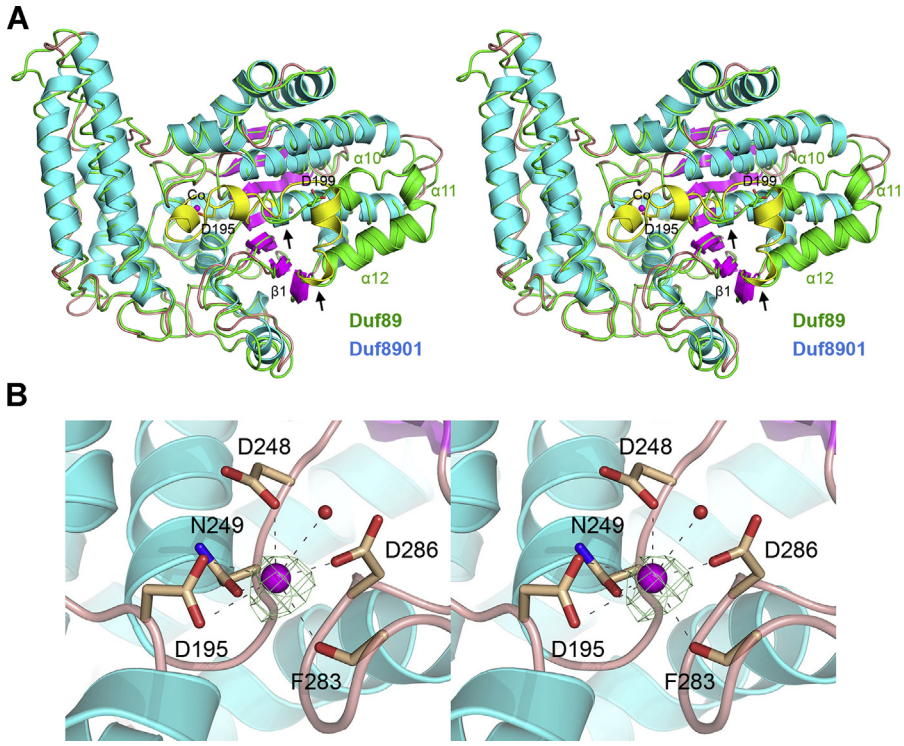

Figure 7. Structure of Duf8901 in complex with cobalt. *A*, stereo view of the tertiary structure of Duf8901, depicted as a *cartoon model* with *magenta β-strands*, *cyan α-helices*, and *blue 3_{10} helices*, superimposed on the tertiary structure of Duf89, depicted as *green ribbon trace*. The two structures differ with respect to the position of their α-10,11,12 "lid" modules. The margins of the lid module are indicated by *arrows*. The Duf8901 lid overlies the active-site pocket and is rendered as a *yellow cartoon model*. The module in Duf89 is reflected away from the active-site pocket and is depicted as a *green cartoon model* with helices labeled. Lid movement results in a ∼16 Å displacement of Duf8901 Asp195 (*stick model*) vis-à-vis the equivalent Asp199 in Duf89 (*stick model*) that brings Asp195 into the active site adjacent to a cobalt ion (*magenta sphere*). *B*, stereo view of the Duf8901 active site with selected amino acids depicted as *stick models*. Cobalt and an adjacent water are rendered as *magenta* and *red spheres*, respectively. The anomalous difference peak overlying the cobalt is depicted as a *green mesh* contoured at 3σ. Duf89, Domain of Unknown Function 89; Duf8901, Domain of Unknown Function 8901.

catalysis is characteristic of the DxDxT family of phosphohydrolase and phosphotransferase enzymes, named for the conserved active-site motif, wherein the first aspartate acts as the catalytic nucleophile. Whereas the chemical lability of an aspartyl–phosphate adduct makes it difficult to capture the phosphoenzyme intermediate, it has been possible to trap a mimetic of the intermediate by reacting DxDxT enzymes with beryllium chloride and sodium fluoride in the presence of divalent cation, so that the enzyme forms a covalent BeF_3 adduct to the catalytic aspartate that is resistant to hydrolysis. Crystal structures have been determined for aspartyl–BeF_3 derivatives of exemplary DxDxT family members phosphoserine phosphatase (10), CTD protein phosphatases Scp1 and Fcp1 (11, 12), fungal trehalose-6-phosphate phosphatase (13), and phage T4 polynucleotide 3′-phosphatase www.rcsb.org/structure/5UJ0.

At present, there is no experimental evidence that DUF89 enzymes form a covalent intermediate. To address this knowledge gap, we captured an analog of the covalent phosphoenzyme intermediate by crystallizing Duf8901 that had been preincubated in the presence of $BeCl_2$, NaF, and $CoCl_2$. The structure, solved at 2.16 Å resolution, revealed a covalent bond between Asp248 Oδ1 and the beryllium atom of BeF_3. The Asp–BeF_3 adduct adopts the tetrahedral geometry expected for the imputed aspartyl–phosphate intermediate (Fig. 8*A*). An anomalous difference peak corresponding to the cobalt ion is seen at the center of an octahedral coordination complex (Fig. 8*A*). The six metal ligands are Asp248-Oδ2, Asp286-Oδ1, Asn249-Oδ, two waters, and a fluorine atom of BeF_3 (which mimics a phosphate oxygen) (Fig. 8*A*). The interatomic distances between cobalt and the six metal ligands are 2.0 to 2.2 Å. The metal-bound waters are bridged to the enzyme *via* Asp286-Oδ2, Asp195-Oδ2, and Phe283-O (Fig. 8*A*). The enzyme makes a network of contacts to the three fluorine atoms of BeF_3 and the bridging oxygen to Asp248 (*i.e.*, representing the four phosphate oxygens). The fluorine/phosphate ligands in the aspartyl–BeF_3/phosphate adduct are Lys401-Nζ, Asn192-Nδ, Asn249-Nδ, and the Asp363 and Leu364 main chain amides (Fig. 8*A*). The interatomic distances between the enzyme and the metal-bound waters and the fluorine atoms of BeF_3 are 2.6 to 3.0 Å. A water in the active site is located 4 Å from the beryllium atom in a near-apical orientation to the bridging oxygen of Asp248 (water–Be-Oδ1 angle of 155) and is a plausible mimetic of a water nucleophile for hydrolysis of an aspartyl–phosphate catalytic intermediate.

Structure-guided alanine scan of the Duf8901 active site

We produced and purified a series of Duf8901 mutants in which amino acids Asp248, Asn249, Lys401, Asp286, and Asp195 that interact with BeF_3 or cobalt were changed singly to alanine (Fig. 8*B*). The Duf8901-Ala proteins were tested for

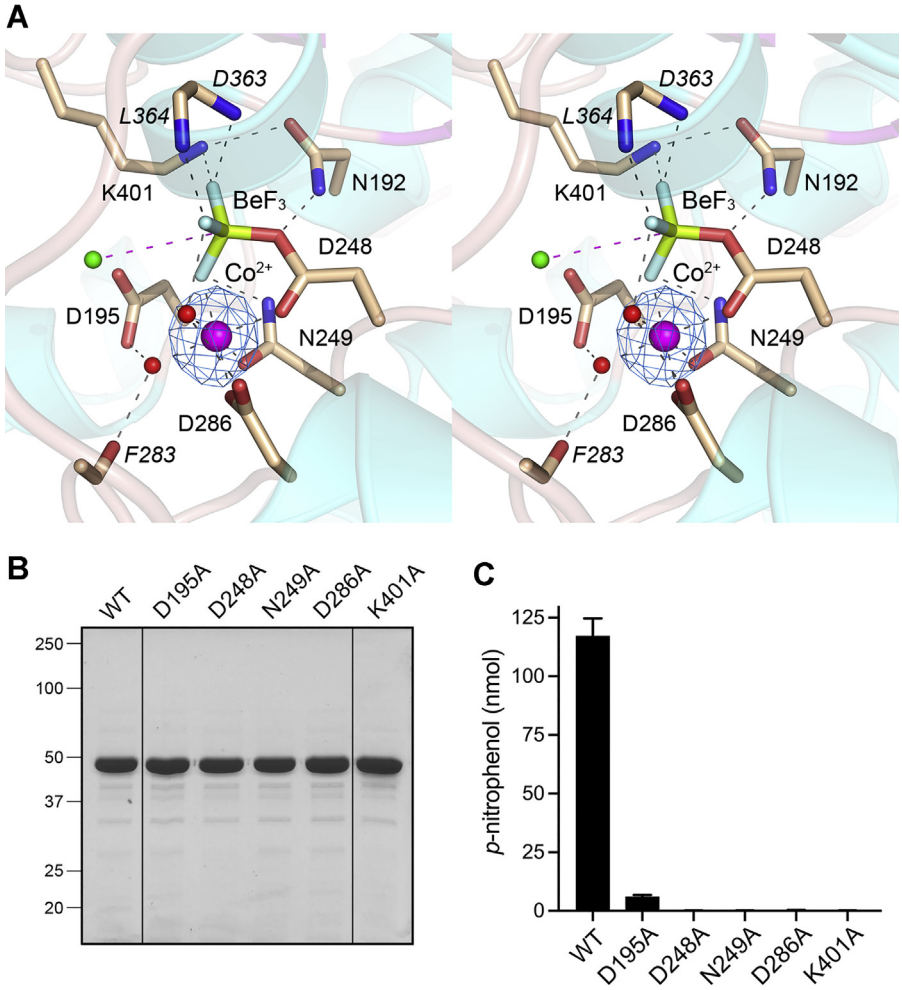

Figure 8. Duf8901 BeF_3 adduct mimics a covalent aspartyl–phosphate intermediate. *A*, stereo view of the active site of the Duf8901-(Asp248)–BeF_3•Co^{2+} structure with selected amino acids depicted as *stick models* with *beige carbons*. Cobalt and two waters in the octahedral metal coordination complex are rendered as *magenta* and *red spheres*, respectively. BeF_3 is depicted with a *yellow–green beryllium atom* and *light blue fluorine atoms*. The anomalous difference peak overlying the cobalt is depicted as a *blue mesh* contoured at 5σ. Atomic contacts of Asp-BeF_3 and the cobalt complex are indicated by *dashed lines*. A water (*green sphere*) adjacent and nearly apical to the BeF_3 adduct is a plausible mimetic of the water nucleophile for hydrolysis of a proposed covalent Duf8901-aspartyl–phosphate intermediate. *B*, structure-guided alanine scan. Aliquots (5 μg) of purified wildtype Duf8901 and the indicated alanine mutants were analyzed by SDS-PAGE. The Coomassie blue–stained gel is shown. The positions and sizes (kilodalton) of marker polypeptides are indicated on the *left*. Note: irrelevant lanes between WT and D195A and between D286A and K401A were deleted from the gel photograph and the flanking lanes were joined; the splice borders are denoted by *vertical lines*. *C*, phosphatase reaction mixtures (50 μl) containing 50 mM Tris-acetate (pH 6.5), 50 mM NaCl, 10 mM (500 nmol) *p*-nitrophenylphosphate, 0.5 mM $CoCl_2$, and 1 μM (50 pmol) of WT or mutant Duf8901 were incubated at 37 °C for 30 min. The extents of *p*-nitrophenol production are plotted. Data are the averages of three independent experiments ± SEM. BeF_3, beryllium trifluoride; Duf8901, Domain of Unknown Function 8901.

p-nitrophenylphosphatase activity in parallel with wildtype Duf8901. Activity was eliminated by the D248A, N249A, D286A, and K401A mutations (≤0.2% of wildtype) and reduced to 5% of wildtype by the D195A change (Fig. 8*C*).

Nickel and zinc support Asp–BeF_3 adduct formation

Because nickel and zinc are also effective cofactors for the phosphomonoesterase activity of Duf8901 (Fig. 4*B*), we tested their ability to replace cobalt in promoting formation of the aspartyl–BeF_3 adduct, by crystallizing Duf8901 that had been preincubated in the presence of $BeCl_2$, NaF, and either $NiCl_2$ or $ZnCl_2$. Diffraction data collected at the nickel and zinc absorption peak wavelengths were used to solve structures of the Duf8901-(Asp248)–BeF_3•Ni^{2+} and Duf8901-(Asp248)–BeF_3•Zn^{2+} adducts at a resolution of 2.1 Å (Table S3). The active sites of the BeF_3•Ni^{2+} and BeF_3•Zn^{2+} structures are shown in Figure 9, *A* and *B*, with anomalous difference peaks over the nickel and zinc ions contoured at 28σ and 12σ, respectively. The nickel and zinc coordination complexes and the enzymic interactions with metals and BeF_3 (Fig. 9, *A* and *B*) are virtually identical to those seen in the Duf8901-(Asp248)–BeF_3•Co^{2+} complex (Fig. 8*A*). This ensemble of aspartyl–BeF_3 structures with three different "active" metals fortifies the case for a covalent aspartyl–phosphate intermediate.

Replacing the aspartate nucleophile with asparagine abolishes Duf89 and Duf8901 activity

Because the Asp248 side chain in Duf8901 does double duty—with one Oδ acting as the nucleophile for covalent catalysis and the other Oδ coordinating the metal cofactor

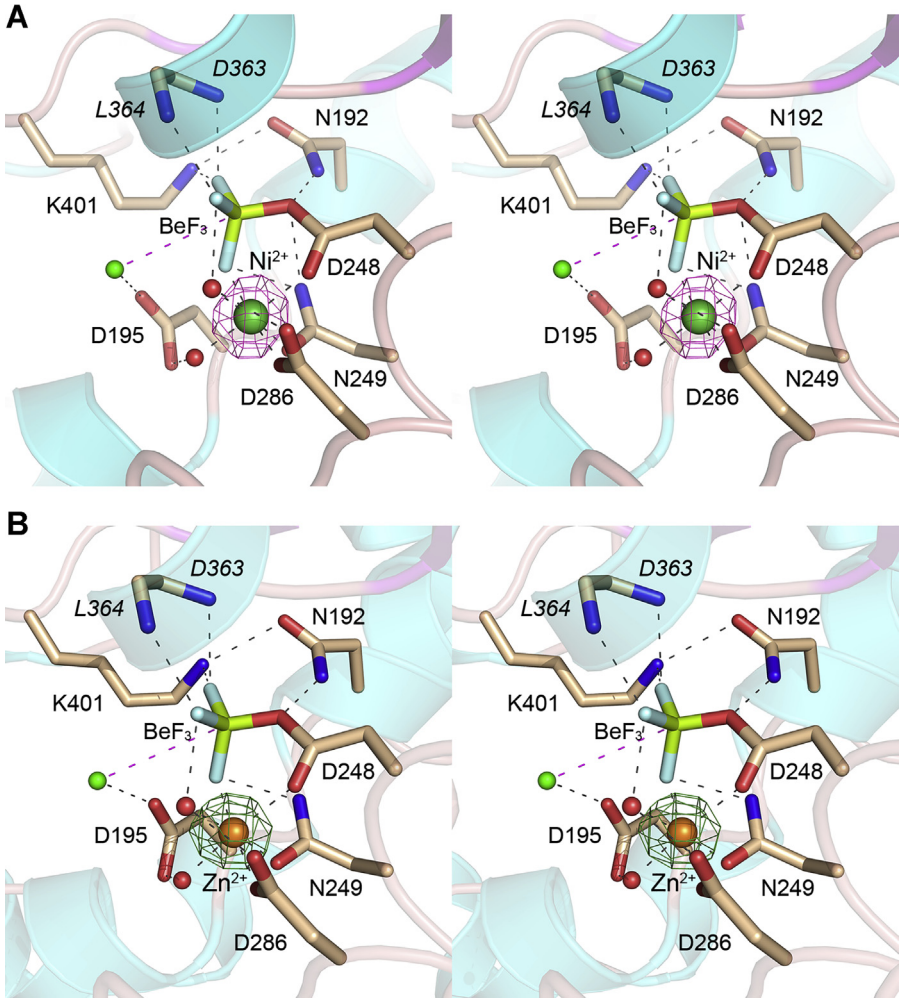

Figure 9. Structures of Duf8901-(Asp248)–BeF_3•Ni^{2+} and Duf8901–(Asp248)–BeF_3•Zn^{2+} adducts. Stereo view of the active site of the Duf8901-(Asp248)–BeF_3•Ni^{2+} (*A*) and Duf8901-(Asp248)–BeF_3•Zn^{2+} (*B*) structures with selected amino acids depicted as *stick models*. Nickel and zinc are rendered as *green* and *gold spheres*, respectively. Two waters in the octahedral metal coordination complex are depicted as *red spheres*. BeF_3 is depicted with a *yellow–green beryllium atom* and *light blue fluorine atoms*. The anomalous difference peak overlying the nickel is depicted as a *magenta mesh* contoured at 28σ. The anomalous difference peak overlying the zinc is depicted as a *green mesh* contoured at 12σ. Atomic contacts of Asp–BeF_3 and the metal complexes are indicated by *dashed lines*. A water (*green sphere*) adjacent to the BeF_3 adduct is a plausible mimetic of the water nucleophile. BeF_3, beryllium trifluoride; Duf8901, Domain of Unknown Function 8901.

(Figs. 8*A* and 9)—the finding that mutating Duf8901 Asp248 to alanine and Duf89 Asp252 to alanine eliminates phosphatase activity does not report directly on the essentiality of aspartate as nucleophile. To approximate this issue, we introduced asparagine in lieu of Duf8901 Asp248 and Duf89 Asp252, a conservative single-atom modification that is isosteric to aspartate, capable in principle of coordinating the metal cofactor *via* Oδ but unable to form a covalent phosphoenzyme *via* Nδ. The recombinant Duf8901 D248N and Duf89 D252N proteins were purified (Fig. 10*A*) and tested for *p*-nitrophenylphosphatase activity in parallel with wildtype Duf8901 and Duf89. The asparagine mutations effaced phosphatase activity in both cases (Fig. 10*B*).

Structure of a Duf8901-(Asp248)–AlF_4 transition state mimetic

We captured an AlF_4 analog of the transition state of the hydrolysis reaction by crystallizing Duf8901 that had been preincubated in the presence of $AlCl_3$, NaF, and $CoCl_2$. The structure, solved at a resolution of 1.8 Å, revealed that AlF_4 adopts a square bipyramidal geometry with a water nucleophile and the Asp248-Oδ-leaving group at the apices, equidistant from the aluminum center—1.8 Å for water and 1.9 Å for Asp248-Oδ—and with a water–Al–Oδ angle of 175° (Fig. 11). The distances and geometry are consistent with an associative in-line mechanism of phosphoryl transfer. The cobalt ion (shown in Fig. 11 with its overlying anomalous difference peak contoured at 32σ) is engaged octahedrally in the bipyramidal transition state mimetic to the same six ligands (cobalt to ligand distances of 1.9–2.1 Å) as seen in the tetrahedral BeF_3 adduct: Asp248-Oδ, Asp286-Oδ, Asn249-Oδ, two waters, and a fluorine atom of AlF_4 (in lieu of a fluorine in BeF_3) (Fig. 11). The planar fluorine atoms of AlF_4 and the Asp248-Oδ-leaving group receive the same enzymic contacts from Lys401-Nζ, Asn192-Nδ, Asn249-Nδ, and the Asp363 and Leu364 main chain amides (Fig. 11; interatomic distances of 2.5–3.0 Å) as their counterparts in the BeF_3 structure. A salient

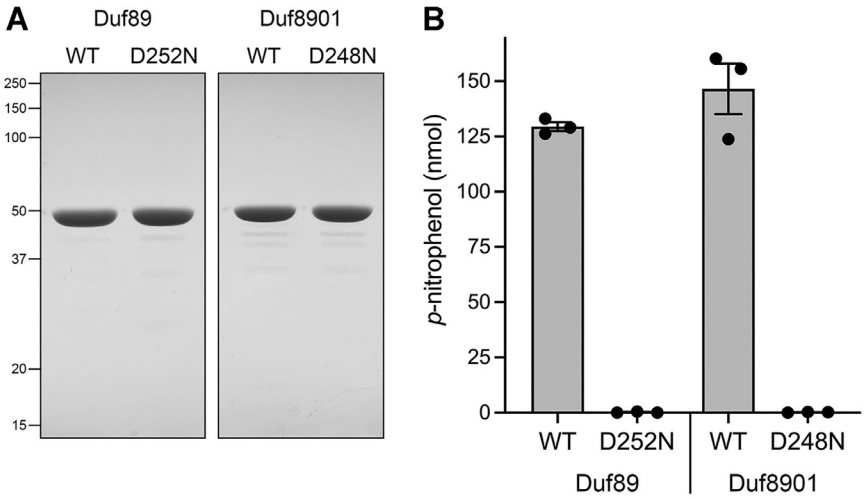

Figure 10. Replacing the aspartate nucleophile with asparagine abolishes Duf89 and Duf8901 activity. *A*, aliquots (5 μg) of purified wildtype Duf89, Duf89-D252N, wildtype Duf8901 and Duf8901-D248N were analyzed by SDS-PAGE. The Coomassie blue–stained gel is shown. The positions and sizes (kilodalton) of marker polypeptides are indicated on the *left*. *B*, phosphatase reaction mixtures (50 μl) containing 50 mM Tris-acetate (pH 6.5), 50 mM NaCl, 10 mM (500 nmol) *p*-nitrophenylphosphate, 0.5 mM $CoCl_2$, and either 0.6 μM (30 pmol) of Duf89 or 1 μM (50 pmol) of Duf8901 proteins as specified were incubated at 37 °C for 30 min. The extents of *p*-nitrophenol production are plotted. Data are the averages of three independent experiments ± SEM, Duf89, Domain of Unknown Function 89; Duf8901, Domain of Unknown Function 8901.

feature of the transition state vis-à-vis the covalent intermediate is the unambiguous assignment of the water nucleophile (*red water sphere* in Fig. 11 *versus* the *"green" water spheres* in Figs. 8*A* and 9). The candidate water surmised from the BeF_3 structures has closed the distance to the aluminum (*i.e.*, the phosphorus) in the transition state and is poised apically for catalysis. Coupled to this transition, the water nucleophile is engaged by Asp195-Oδ and Asp363-Oδ, each situated 2.9 Å from the water oxygen (Fig. 11). Whereas Asp195 was seen to coordinate the "out of position" green water in the BeF_3 structures, the Asp363 side-chain carboxylate was pointing away from BeF_3 at a distance of 4.7 Å from the green water. Compared with the covalent intermediate, the transition state Asp363 side chain has undergone a rotation about Cα–Cβ that

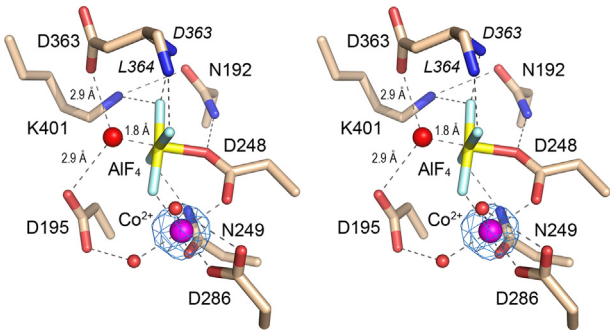

Figure 11. Structure of a Duf8901-(Asp248)–AlF_4 transition state mimetic. Stereo view of the active site of the Duf8901-(Asp248)–AlF_4–OH_2•Co^{2+} structure with selected amino acids depicted as *stick models*. Cobalt and two waters in the octahedral metal coordination complex are rendered as *magenta and red spheres*, respectively. AlF_4 is depicted with a *yellow aluminum atom* and *light blue fluorine atoms*. The anomalous difference peak overlying the cobalt is depicted as a *blue mesh* contoured at 32σ. Atomic contacts of Asp-AlF_4 and the cobalt complex are indicated by *dashed lines*. The water nucleophile for hydrolysis of aspartyl phosphate—situated 1.8 Å from the aluminum and almost perfectly apical to the Asp248-Oδ-leaving atom—is coordinated by Asp195-Oδ and Asp363-Oδ. AlF_4, aluminum fluoride; Duf8901, Domain of Unknown Function 8901.

results in a ∼3.1 Å movement of Oδ that enables its coordination of the water nucleophile. Dual hydrogen bonds from the water nucleophile to Asp195 and Asp363 serve to orient it for attack on aspartyl phosphate and to provide for activation of the water *via* general base catalysis.

Distinctive effects of duf89 *and* duf8901 *deletion on Pho1 expression*

We constructed fission yeast *duf89*Δ and *duf8901*Δ strains as well as a *duf89*Δ *duf8901*Δ double mutant. Spot testing for growth on YES agar showed that *duf89*Δ, *duf8901*Δ, and *duf89*Δ *duf8901*Δ cells grew as well as a wildtype strain (Fig. 12*A*). We then assayed *pho1* expression during exponential growth at 30 °C in liquid culture under phosphate-replete conditions (Fig. 12*B*). Cell surface–associated Pho1 acid phosphatase activity (a gauge of Pho1 enzyme level that correlates with *pho1* mRNA levels) was quantified by incubating suspensions of serial dilutions of the cells for 5 min with *p*-nitrophenylphosphate and assaying colorimetrically the formation of *p*-nitrophenol. The basal Pho1 activity of wildtype cells was derepressed by ninefold in *duf89*Δ cells (Fig. 12*B*), thus affirming the finding of Henry *et al.* (5). By contrast, the *duf8901*Δ allele had no effect *per se* on Pho1 expression and did not impact the derepression of Pho1 elicited by *duf89*Δ (Fig. 12*B*). We infer that Duf8901 and Duf89 are neither functionally equivalent nor functionally redundant with respect to vegetative growth; nor are they functionally equivalent with regard to involvement in phosphate homeostasis.

Discussion

DUF89-family metal-dependent phosphohydrolases are prevalent in all phylogenetic domains and presently grouped into three subfamilies (1). The DUF89 enzymes characterized

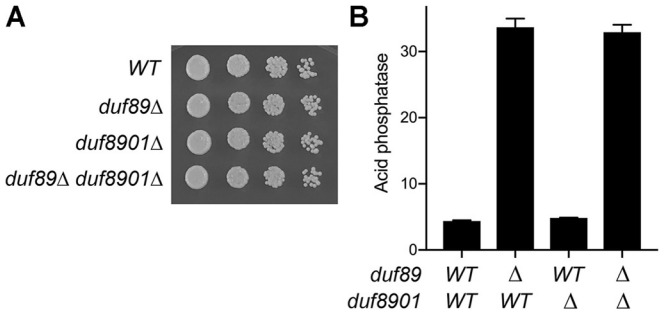

Figure 12. Duf8901 is a paralog of Duf89 but not a functional ortholog. *A*, wildtype, *duf89*Δ, *duf8901*Δ, and *duf89*Δ *duf8901*Δ strains were spot tested for growth on YES agar at 30 °C. *B*, the indicated strains were assayed for Pho1 acid phosphatase activity. Duf89, Domain of Unknown Function 89; Duf8901, Domain of Unknown Function 8901.

to date display relatively vigorous activity with *p*-nitrophenylphosphate (vis-à-vis other substrates tested). Individual DUF89 enzymes differ in their metal cofactor and substrate preferences, as gauged by biochemical screening of exemplary members of each DUF89 subfamily for their ability to hydrolyze a panel of 95 additional phosphosubstrates, primarily low–molecular weight compounds, such as sugars, nucleotides, amino acids, and vitamin derivatives (1). It is proposed that DUF89 enzymes act as scavengers to limit the intracellular accumulation of deleterious or damaged phosphometabolites (1). However, establishing the true nature of the *in vivo* targets of DUF89 activity and biological contexts in which DUF89 enzymes might be important (*e.g.*, an overt cellular phenotype elicited by DUF89 deficiency) remains challenging. Informative structures have been reported for several DUF89 proteins, including as complexes with a divalent cation—either magnesium or manganese, neither of which is optimal for activity. Nonetheless, the catalytic mechanism of DUF89 enzymes is not well understood.

The present study provides new insights into DUF89 mechanism and repertoire *via* characterization of two subfamily III DUF89 paralogs—Duf89 and Duf8901—from the fission yeast *S. pombe*. Hydrolysis of *p*-nitrophenylphosphate by Duf89 and Duf8901 relies on nickel or cobalt as the divalent cation cofactor. Their apparent k_{cat} values (Duf89: 9.7 s^{-1}; Duf8901: 2.9 s^{-1}) are similar to, or several-fold greater than, those reported for *p*-nitrophenylphosphate hydrolysis by human, plant, and archaeal DUF89 proteins (1, 4). A new finding here is that Duf89 is also adept at cobalt/nickel-dependent hydrolysis of PP_i (k_{cat} 32 min^{-1}). Whereas pyrophosphate was included in the panel of 96 substrates used by Huang *et al.* (1) to screen exemplary DUF89 enzymes, their report did not mention pyrophosphatase activity as an attribute of the DUF89 proteins studied, with the exception of *Pyrococcus* DUF89, for which their data indicated little or no pyrophosphate hydrolysis. That the apparent K_m of fission yeast Duf89 for PP_i was 10-fold lower than its K_m for *p*-nitrophenylphosphate might signal that it acts on one or more pyrophosphorylated metabolites, though that remains speculative at present. Pyrophosphate hydrolysis appears not to be an isolated property of fission yeast Duf89, insofar as Duf8901 also has a nickel/cobalt-dependent inorganic pyrophosphatase activity, as does the human DUF89 homolog.

Our determination of crystal structures of the fission yeast DUF89 paralogs highlights several key points regarding DUF89 mechanism. First, we unveil a mobile structural module of subfamily III DUF89 proteins, comprising Duf89 helices 10,11,12 and the corresponding helices in Duf8901. This lid-like module is reflected away from the active-site pocket in the metal-free Duf89 structure and closes over the active-site pocket in the metal-bound Duf8901 structures. The lid closure results in a ∼16 Å movement of Duf8901 Asp195 vis-à-vis the equivalent Asp199 in Duf89 that incorporates Asp195 into an octahedral cobalt coordination complex *via* a bridging water. We regard the closed state of the protein as being on-pathway insofar as this is the conformation seen in the cobalt-coordinated BeF_3 mimetic of a covalent aspartyl–phosphate intermediate. Because the lid closure appears to occlude access to the active-site pocket, we infer that the open conformation seen in the Duf89 structure approximates a state permissive for entry of phosphosubstrate and metal into the active-site pocket, after which lid closure is triggered. The dynamic nature of the lid is underscored by the fact that this segment (and its counterpart of metal-binding Asp199) is disordered in the budding yeast, human, and plant DUF89 structures. In the case of the *Pyrococcus* DUF89 structure (PDB ID: 2G8L), the lid is visualized in an intermediate position relative to Duf89 (wide open) and Duf8901 (closed), whereby the Cα atom of Asp111 is displaced by 6.1 Å from that of Duf8901 Asp195. Presumably, the lid reopens after catalysis to allow product release. It is not clear whether the crystallization of a closed complex of Duf8901 in the presence of cobalt results because the metal promotes module closure, *versus* the crystallization conditions *per se* favoring this conformation as opposed to that of Duf89. (Note that Duf89 and Duf8901–BeF_3 crystallized under different conditions and their respective crystal lattices differed with respect to the number of protomers in the ASU.)

The structures of Duf8901 as an aspartyl–BeF_3 adduct and an aspartyl–AlF_4-OH_2 adduct instate a mechanism of covalent catalysis for this DUF89 enzyme, one that we suspect applies to all DUF89 family members, regardless of what their preferred phosphosubstrates might be. For Duf8901, we propose a two-step reaction pathway entailing: (i) nucleophilic attack of Asp248 on the phosphorus of an R–O–PO_3 substrate, resulting in the formation of a covalent enzyme–aspartyl–phosphate intermediate and an R–OH product and (ii) hydrolysis of the aspartyl phosphate to release P_i product. Both steps likely proceed in-line *via* a pentacoordinate phosphorane transition state in which the nucleophile and leaving atoms occupy the apices of the trigonal bipyramid. AlF_4^- complexes have been instrumental in obtaining structural snapshots of transition state analogs of enzymic phosphoryl transfer enzymes in which the anionic square planar AlF_4 mimics the trigonal planar configuration of the scissile phosphate (14). In our structure of the Duf8901-(Asp248)–AlF_4-OH_2 complex, AlF_4 forms a square bipyramid with a water nucleophile and the Asp248-Oδ leaving group at the apices. The water–Al and Al–Oδ distances and geometry implicate an associative in-line mechanism of phosphoryl transfer.

The Duf8901 aspartyl–BeF_3 and aspartyl–AlF_4 structures suggest that the transition state is stabilized by electrostatic and polar contacts to the nonbridging phosphate oxygens made by Lys401 and Asn249 and by the divalent cation cofactor. In principle, we can invoke general acid–base catalysis as a component of the DUF89 mechanism, whereby an enzymic general acid donates a proton to the R–OH leaving group during step 1 and a general base accepts a proton from the water nucleophile during step 2. In the case of DxDxT family phosphotransferases that act *via* a covalent aspartyl–phosphate intermediate, the second Asp of the DxDxT motif is proposed to act sequentially as general acid and general base. Huang *et al.* (1) had suggested that Asp292 in budding yeast YMR027W (corresponding to Asp286 in Duf8901) could activate the water nucleophile during the phosphohydrolase reaction. Based on the Duf8901-(Asp248)–AlF_4-OH_2 transition-state structure (in which water is poised for catalysis), we feel this is most unlikely, insofar as Asp286 is coordinating a metal-bridged water that is 3.8 Å from the aluminum atom and orthogonal to the leaving Asp248-Oδ atom of the aspartyl–AlF_4 adduct (water–Al–Asp248-Oδ angle of 84). Rather, we propose that Asp195 and Asp363, acting singly or in concert, take the role of general base catalyst of the hydrolysis reaction. Asp195-Oδ and Asp363-Oδ are equidistant (2.9 Å) from the water nucleophile, in position to accept bifurcated hydrogen bonds from the water that orient the water for its attack on the scissile phosphate and allow for its deprotonation by transfer to an Asp-Oδ. We envision that the R–O leaving group in the transition state of the first step of the Duf8901 pathway occupies the same position as the water nucleophile in the Duf8901-(Asp248)–AlF_4-OH_2 transition state, and that analogous interactions of Asp195 and Asp363 (one or both of which are protonated) with the R–O leaving atom allows for general acid catalysis of R–OH product expulsion. Asp195 and Asp363 are conserved among DUF89 family members. We show here by alanine mutation that Asp195 is critical for Duf8901 *p*-nitrophenylphosphatase activity. Huang *et al.* (1) reported that alanine mutation of the counterpart of Duf8901 Asp363 in budding yeast YMR027W (Asp384) abolished *p*-nitrophenylphosphatase activity.

With respect to fission yeast Duf89, it is noteworthy that the site occupied by phosphate in the Duf89•PO_4 structure is not what one would expect for either the hydrolyzed phosphate product of step 2 or (potentially) the phosphate leaving group derived by step 1 reaction with PP_i. It is possible that the hydrolyzed phosphate migrates to the position after step 2 chemistry; alternatively, phosphate occupancy of this site is off pathway and occurs during Duf89 crystallization at pH 5.

Given our new appreciation that Duf8901 shares with DxDxT-family phosphotransferases the formation of a covalent enzyme-(aspartyl)–phosphate intermediate, we queried whether there is any structural homology underlying this property by performing a pairwise Dali comparison of the Duf8901-(aspartyl)–BeF_3•Co^{2+} structure to the aspartyl–BeF_3•Mg^{2+} structure of the autonomous polynucleotide-3′-phosphatase domain (amino acids 157–300) of T4 polynucleotide kinase phosphatase www.rcsb.org/structure/5UJ0. Dali returned an alignment of the two structures with a relatively low Z score of 3.9, with an rmsd of 3.1 Å at 95 Cα positions that included only 5% amino acid identity. The fold homology embraced a five-strand parallel β-sheet (corresponding to Duf8901 β4↑•β3↑•β2↑ •β5↑•β6↑ in the view shown in Fig. 13*A*) and an α-helix. In both enzymes, the aspartyl–BeF_3 adducts that define the active site are located within a loop immediately following the middle β-strand of the sheet. However, the respective BeF_3 adducts and the metals are not coincident in the structure-based alignment. (Dali aligns Duf8901 Asp248 to T4 Asp167, the second Asp in the DxDxT motif.) Moreover, the aspartyl–BeF_3 moieties are oppositely oriented with respect to the metals in Duf8901 *versus* T4 3′-phosphatase (Fig. 13*A*). To gauge the extent to which the active sites might be conserved, we superimposed them with respect to the respective BeF_3•metal complexes (Fig. 13*B*). Whereas four of the six constituents of the octahedral metal complexes are spatially conserved (BeF_3-F; Asp248/165-O; Asp286/278-O; water), two are distinct. To wit: (i) the direct contact of Asn249-Oδ to cobalt in Duf8901 is a water-bridged contact to magnesium *via* Asp277 in T4 3′-phosphatase and (ii) the position of a water-engaging cobalt in Duf8901 is taken by the Asp167 main chain amide in T4 3′-phosphatase (Fig. 13*B*). Most notable is that none of the contacts to the phosphate oxygen equivalents of the BeF_3 adducts are conserved between Duf8901 and T4 3′-phosphatase. In particular, there are no equivalents of essential Duf8901 residues Lys401 and Asp195 in T4 3′-phosphatase. We surmise that DUF89 and DxDxT enzymes share a Rossmanoid fold β-sheet but are not descendants of a common ancestor.

We also queried the relatedness of Duf8901 to *Salmonella* CheY, a bacterial signal transduction protein and phosphohydrolase that has been captured structurally as a covalent CheY-(aspartyl)–BeF_3 adduct (15). Phosphorylation of the CheY Asp57 side chain by kinase CheA dictates the direction of bacterial flagellar rotation. CheY phosphorylation is short lived because CheY itself catalyzes aspartyl–phosphate hydrolysis. Dali returned an alignment of Duf8901 and *Salmonella* CheY structures with an Z score of 4.0 (rmsd of 3.5 Å at 83 Cα positions) that included 11% amino acid identity. The fold homology embraced a four-strand parallel β-sheet (corresponding to Duf8901 β3•β2 •β5•β6) and an α-helix. However, the respective aspartyl–BeF_3 adducts that define the active site are located on different β-strands of the sheet (Fig. S4*A*). Superposition of the structures with respect to their Asp–BeF_3•metal complexes showed that the active-site architectures are dissimilar (Fig. S4*B*). Other than sharing a Rossmanoid fold, we conclude that Duf8901 and CheY are not derived from a common ancestral enzyme.

Whereas our present biochemical and structural studies of the fission yeast DUF89 paralogs do not reveal their physiological substrates (or the basis for substrate recognition), the distinct effects of their respective gene deletions on the expression of the phosphate homeostasis enzyme Pho1 would suggest that Duf89 and Duf8901 act on different phosphosubstrates *in vivo*, such that only Duf89 deletion derepresses Pho1 expression in phosphate-replete cells. Recent studies have shown that fission yeast Pho1 expression is subject to regulation

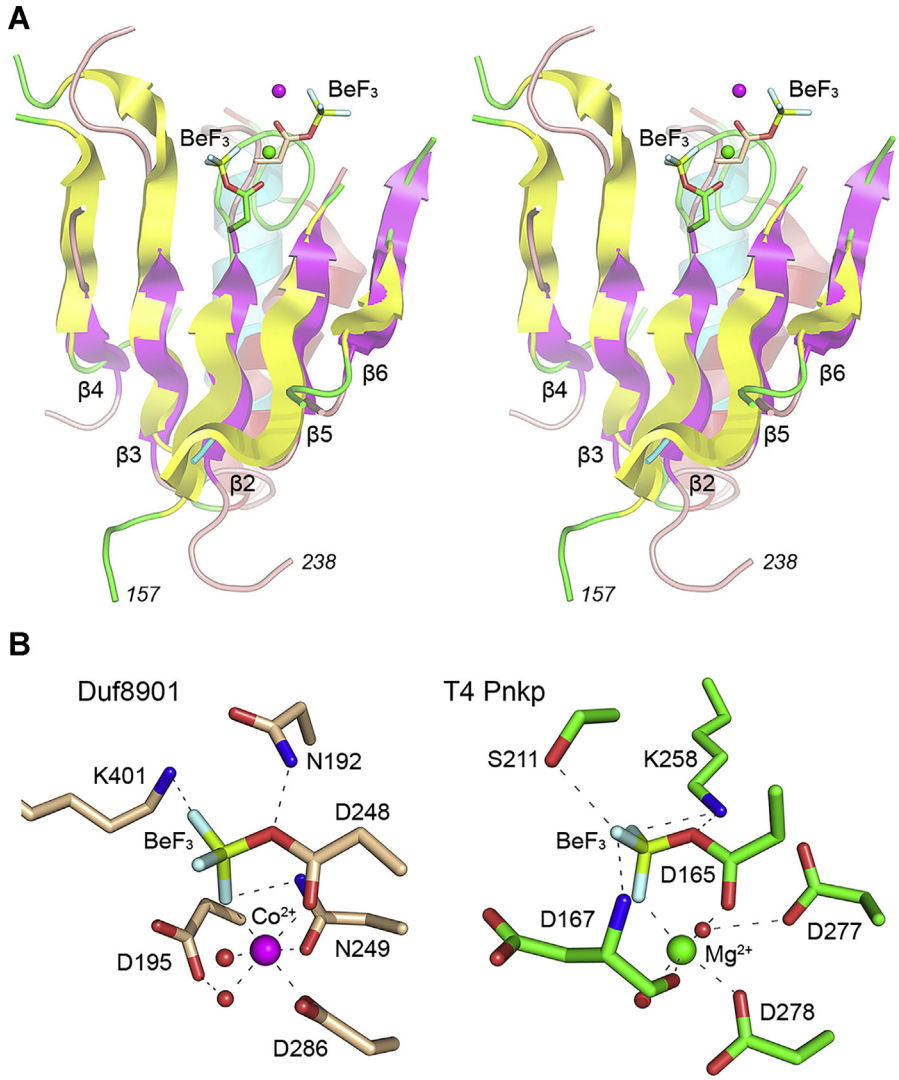

Figure 13. Alignments of Duf8901 and T4 polynucleotide 3′-phosphatase. *A*, pairwise Dali comparison identified a segment of tertiary structure similarity (with scant primary structure conservation) corresponding to the respective five-strand parallel β-sheets. A stereo view of the superimposed folds is shown. Duf8901 is depicted as a *cartoon model* with *magenta β-strands* (labeled as in Fig. 6) and a *cyan α-helix* (corresponding to α14 in Fig. 6). The cobalt ion is a *magenta sphere*. T4 3′-phosphatase is rendered as a *cartoon model* with *yellow β-strands* and a *red α-helix*. The magnesium ion is a *green sphere*. The respective aspartyl-BeF_3 adducts are depicted as *stick models*. *B*, distinct active-site arrangements. The active sites were superimposed with respect to their respective aspartyl-BeF_3 adducts and divalent cations, then offset horizontally. BeF_3, beryllium trifluoride; Duf8901, Domain of Unknown Function 8901.

by the IPP signaling molecule IP8, whereby inactivation of pyrophosphatase enzymes that hydrolyze IP8 leads to Pho1 derepression (8). Moreover, too much IP8 is cytotoxic to fission yeast (16). Pho1 is also derepressed when fission yeast cells are starved for thiamine (the precursor of the essential enzyme cofactor thiamine pyrophosphate) or by mutations in enzymes involved in thiamine metabolism (17, 18). Thus, we can speculate that Duf89 might aid in limiting the accumulation of potentially harmful metabolites in the IPP or thiamine pathways.

Experimental procedures

Recombinant S. pombe *Duf89*

The ORF encoding full-length Duf89 was PCR amplified from *S. pombe* complementary DNA (cDNA) with primers that introduced a BamHI site immediately flanking the start codon and a XhoI site downstream of the stop codon. The PCR product was digested with BamHI and XhoI and inserted between the BamHI and XhoI sites of pET28b-His_{10}Smt3 to generate a T7 RNA polymerase–based expression plasmid encoding the Duf89 polypeptide fused to an N-terminal His_{10}Smt3 tag. Single mutations D252A, D290A, and D252N were introduced into the expression plasmid by two-stage overlap extension PCR with mutagenic primers. All plasmid inserts were sequenced to exclude the presence of unwanted mutations. Wildtype and mutant pET28b-His_{10}Smt3-Duf89 plasmids were transfected into *E. coli* BL21(DE3) cells. Cultures (1 l) amplified from single kanamycin-resistant transformants were grown at 37 °C in Terrific Broth containing 50 μg/ml kanamycin until the absorbance reached 0.75 to 0.8 at 600 nm. The cultures were chilled on ice for 1 h, adjusted to 2.2% (v/v) ethanol and 0.5 mM IPTG, and then incubated for 17.5 h at 17 °C with constant shaking. Cells were harvested by centrifugation and stored at −80 °C. All subsequent steps were

performed at 4 °C. Cells were thawed and resuspended in 25 ml of buffer L (50 mM Tris–HCl [pH 7.5], 500 mM NaCl, 25 mM imidazole, and 10% glycerol). Lysozyme was added to a concentration of 1 mg/ml. After incubation for 30 min, the lysate was sonicated, and the insoluble material was removed by centrifugation at 14,000 rpm for 30 min. The supernatant was mixed for 1.5 h with 2 ml of Ni–nitrilotriacetic acid agarose resin (Qiagen) that had been equilibrated with buffer L. The resin was recovered by centrifugation and washed twice with 30 ml of buffer L. The resin was centrifuged again, resuspended in 20 ml of buffer L, and poured into a column. After washing the column with 20 ml of buffer L, the bound material was eluted with 6 ml of buffer L containing 300 mM imidazole. The polypeptide compositions of the flow-through and eluate fractions were monitored by SDS-PAGE. The 300 mM imidazole eluate fractions containing His_{10}-Smt3-Duf89 were supplemented with Smt3-specific protease Ulp1 (Ulp1/His_{10}-Smt3-Duf89 ratio of 1:425 [w/w]) and then dialyzed overnight against 2 l of buffer L. The dialysates were mixed for 1.5 h with 2 ml of Ni-nitrilotriacetic acid agarose resin that had been equilibrated with buffer L. Tag-free Duf89 proteins were recovered in the flow-through factions. Protein concentrations were determined with Bio-Rad dye reagent using bovine serum albumin as the standard. The yields of wildtype Duf89, Duf89-D252A, Duf89-D290A, and Duf89-D252N were 24, 20, 19, and 26 mg per liter of bacterial culture, respectively.

For protein crystallization, the tag-free Duf89 preparation was concentrated by centrifugal ultrafiltration (Amicon Ultra-15; 10 kDa cutoff) to 21 mg/ml (in 2 ml) and then further purified by gel filtration through a 125-ml 16/60 HiLoad Superdex 200 column (GE Healthcare) equilibrated in 20 mM Tris–HCl, pH 7.5, 150 mM NaCl at a flow rate of 0.5 ml/min while collecting fractions of 2 ml. The peak Duf89 fractions were pooled and concentrated by centrifugal ultrafiltration (Amicon Ultra-15; 30 kDa cutoff) to 24 mg/ml. Protein concentration was determined from the absorbance measured at 280 nm with a Nanodrop spectrophotometer (Thermo Scientific) applying a molar extinction coefficient of 79,090 M^{-1}/cm as calculated by Protparam.

Recombinant S. pombe *Duf8901*

The ORF encoding full-length Duf8901 was PCR amplified from *S. pombe* cDNA with primers that introduced a BamHI site immediately flanking the start codon and a XhoI site downstream of the stop codon. The PCR product was digested with BamHI and XhoI and inserted between the BamHI and XhoI sites of pET28b-His_{10}Smt3 to generate a T7 RNA polymerase–based expression plasmid encoding the Duf8901 polypeptide fused to an N-terminal His_{10}Smt3 tag. Single mutations D195A, D248A, N249A, D286A, K401A, and D248N were introduced into the expression plasmid by two-stage overlap extension PCR with mutagenic primers. All plasmid inserts were sequenced to exclude the presence of unwanted mutations. Recombinant wildtype and mutant Duf8901 proteins were produced in *E. coli* BL21(DE3) and purified from a soluble extract of a culture of 1 l as described previously for *S. pombe* Duf89. The yields of wildtype Duf8901, Duf8901-D195A, Duf8901-D248A, Duf8901-N249A, Duf8901-D286A, Duf8901-K401A, and Duf8901-D248N were 40, 50, 40, 49, 45, 41, and 28 mg per liter of bacterial culture, respectively. For protein crystallization, the tag-free Duf8901 preparation was concentrated by centrifugal ultrafiltration (Amicon Ultra-15; 10 kDa cutoff) to 12 mg/ml (in 2 ml) and then further purified by gel filtration through a 125 ml 16/60 HiLoad Superdex 200 column (GE Healthcare) equilibrated in 20 mM Tris–HCl, pH 7.5, 150 mM NaCl at a flow rate of 0.5 ml/min while collecting fractions of 2 ml. The peak Duf8901 fractions were pooled and concentrated by centrifugal ultrafiltration (Amicon Ultra-15; 30 kDa cutoff) to 20 mg/ml. Protein concentration was determined from the absorbance at 280 nm measured with a Nanodrop spectrophotometer (Thermo Scientific) applying a molar extinction coefficient of 83,685 M^{-1}/cm, as calculated by Protparam.

Recombinant human DUF89

A synthetic cDNA clone for the C6orf211 ORF, codon optimized for expression in *E. coli* and containing a BamHI site immediately flanking the start codon and a XhoI site downstream of the stop codon, was purchased from Genscript. The ORF was excised with BamHI and XhoI and inserted between the BamHI and XhoI sites of pET28b-His_{10}Smt3. Recombinant human DUF89 was produced in *E. coli* BL21(DE3) and purified from a soluble extract of a culture of 1 l as described previously for *S. pombe* Duf89. The yield of tag-free human DUF89 was 8 mg.

Hydrolysis of p*-nitrophenylphosphate*

Reaction mixtures (50 μl) containing 50 mM Tris-acetate (pH 6.5), 50 mM NaCl, 10 mM (500 nmol) *p*-nitrophenylphosphate, 0.5 mM divalent cation, and DUF89 proteins as specified were incubated at 37 °C. The reactions were quenched by adding 5 μl of 100 mM EDTA and then 0.95 ml of 1 M Na_2CO_3. Release of *p*-nitrophenol was determined by measuring absorbance at 410 nm and interpolating the value to a *p*-nitrophenol standard curve.

Hydrolysis of PP_i

Reaction mixtures (100 μl) containing 50 mM Tris-acetate (pH 6.5), 25 mM NaCl, 1 mM (100 nmol) sodium pyrophosphate, 0.5 mM divalent cation, and DUF89 proteins as specified were incubated at 37 °C. The reactions were quenched by adding 1 ml of Malachite Green reagent (Enzo Life Sciences) followed by an incubation of 20 min at room temperature. Phosphate release was determined by measuring absorbance at 620 nm and interpolating the value to a phosphate standard curve.

Protein crystallization

Duf8901•Co^{2+} complex

A solution containing 0.3 mM Duf8901, 5 mM $CoCl_2$, 19 mM Tris–HCl (pH 7.5), and 142 mM NaCl was pre-incubated on ice for 15 min. Aliquots (2 μl) were then mixed

with 2 μl of precipitant solution containing 1.8 M sodium phosphate monobasic monohydrate/potassium phosphate dibasic (pH 8.2).

Duf8901-BeF_3•Co^{2+} complex

A solution containing 0.3 mM Duf8901, 5 mM $CoCl_2$, 5 mM $BeCl_2$, 15 mM NaF, 15 mM Tris–HCl (pH 7.5), and 112 mM NaCl was preincubated on ice for 1 h. Aliquots (2 μl) were then mixed with 2 μl of precipitant solution containing 1.8 M sodium phosphate monobasic monohydrate/potassium phosphate dibasic (pH 8.0). Duf8901 crystals were grown by sitting drop vapor diffusion at room temperature. Crystals grew over 1 to 2 days and were harvested 1 day later. The crystals were cryoprotected with 100% paraffin oil and then flash-frozen in liquid nitrogen.

Duf8901-BeF_3•Zn^{2+} complex

A solution containing 0.3 mM Duf8901, 2 mM $ZnCl_2$, 5 mM $BeCl_2$, 15 mM NaF, 15 mM Tris (pH 7.5), and 112 mM NaCl was preincubated on ice for 1 h. Aliquots (2 μl) were then mixed with 2 μl of precipitant solution containing 1.8 M sodium phosphate monobasic monohydrate/potassium phosphate dibasic (pH 8.0). Crystals were grown by sitting drop vapor diffusion at room temperature. Crystals grew over 3 days and were harvested 7 days later. Crystals were cryoprotected with 25% sucrose and then flash-frozen in liquid nitrogen.

Duf8901-BeF_3•Ni^{2+} complex

A solution containing 0.24 mM Duf8901, 5 mM $NiCl_2$, 5 mM $BeCl_2$, 15 mM NaF, 17 mM Tris (pH 7.5), and 127 mM NaCl was preincubated on ice for 1 h. Aliquots (2 μl) were then mixed with 2 μl of precipitant solution containing 1.8 M sodium phosphate monobasic monohydrate/potassium phosphate dibasic (pH 7.8). Streak seeding techniques were used to improve crystal appearance. Crystals were grown by sitting drop vapor diffusion at room temperature and harvested after 5 days. The crystals were cryoprotected with 25% sucrose and then flash-frozen in liquid nitrogen.

Duf8901-AlF_4•Co^{2+} complex

A solution containing 0.3 mM Duf8901, 5 mM $CoCl_2$, 5 mM $AlCl_3$, 15 mM NaF, 17 mM Tris (pH 7.5), 127 mM NaCl, and 0.43 mM EDTA was preincubated on ice for 1 h. Aliquots (0.5 μl) were then mixed with 0.5 μl of precipitant solution containing 0.2 M NaCl, 0.1 M Hepes (pH 7.0), and 20% (w/v) PEG-6000. Crystals were grown by sitting drop vapor diffusion at room temperature. Crystals grew over 1 day and were harvested 5 days later. Crystals were cryoprotected with 25% sucrose and then flash-frozen in liquid nitrogen.

Duf89

A solution containing 0.24 mM Duf89, 5 mM $CoCl_2$, 10 mM sodium pyrophosphate (pH 6.5), 18 mM Tris–HCl (pH 7.5), and 135 mM NaCl was preincubated on ice for 15 min. Aliquots (0.5 μl) were then mixed with 0.5 μl of precipitant solution containing 0.1 M citric acid (pH 5.0) and 20% (w/v) PEG-6000. Duf89 crystals were grown by sitting drop vapor diffusion at room temperature and harvested after 3 days. The crystals were cryoprotected with 100% paraffin oil and then flash-frozen in liquid nitrogen.

Structure determination

Diffraction data were acquired at Argonne National Laboratory beamline ID-24-C or ID-24-E. Reduction of all crystallographic data was performed using XDS (19) and AIMLESS (CCP4 suite) (20). Phasing information was obtained using PHENIX.PHASER suite (21). All structures were iteratively refined in PHENIX.REFINE and manually adjusted in COOT (22). The diffraction and refinement statistics are compiled in Tables S1 and S3.

Duf8901•Co^{2+} structure

Two sets of diffraction data from a single crystal of Duf8901 grown in the presence of Co were collected at a wavelength of 0.9792 Å at beamline 24-ID-E. The crystal diffracted to 2.75 Å and belonged to space group $P22_12_1$ with unit cell dimensions consistent with two or three protomers per ASU, assuming solvent contents of 60% or 40%, respectively. The data were combined, and the structure was determined by molecular replacement (MR) in PHENIX.PHASER using a homology model of Duf89 protein generated in Phyre2 (23) as a search ensemble. PHENIX.PHASER found 1 MR solution with translation function Z (TFZ) and log-likelihood gain (LLG) scores of 24.2 and 480.8, respectively, and two copies of Duf8901 protein in the ASU. A partially refined model was then used to solve a structure of a better-diffracting Duf8901 crystal. Diffraction data at 1.90 Å resolution (collected at a wavelength of 0.9792 Å, henceforward called a native dataset) and 2.16 Å resolution (collected at a wavelength of 1.5895 Å, corresponding to the energy of K-edge absorption for Co^{2+}; henceforward called an anomalous dataset) were obtained from a single crystal of Duf8901 at beamline 24-ID-C. Phases were determined by MR in combination with single-wavelength anomalous dispersion (MR-SAD) in PHENIX.PHASER by using the anomalous dataset with a resolution cutoff of 4 Å and the partially refined 2.75 Å Duf8901 model (devoid of heteroatoms) as a search ensemble. A calculated Duf8901 substructure contained two cobalt atoms, with figure of merit (FOM) and LLG scores of 0.506 and 83.5, respectively. Following density modification in PHENIX.RESOLVE, the initial 2.16 Å model was built, containing two molecules of Duf8901 protein per ASU. The model was subsequently subjected to three macrocycles of refinement, including refinement of the anomalous groups, without imposing non-crystallographic symmetry (NCS) restrains. The resolution was then extended to 1.90 Å by refinement against the native dataset. The Duf8901•Co^{2+} complex was iteratively rebuilt in PHENIX.REFINE in the presence of experimental phase restraints and included translation libration screw (TLS) B-factor refinement (14 TLS groups). The final model refined to R_{work}/R_{free} of 16.4/19.6, with 98.2% of the 871 amino acid residues in the favored regions of the Ramachandran plot and only a single outlier.

Duf8901–BeF_3•Co^{2+} structure

Diffraction data for a single crystal of Duf8901 that had been preincubated with cobalt, $BeCl_2$, and NaF were collected at 1.6060 Å wavelength (cobalt K-edge) at beamline 24-ID-C. The crystal was isomorphous with the Duf8901•Co^{2+} crystal and diffracted to a resolution of 2.16 Å. MR-SAD phases were calculated in PHENIX.PHASER by combining anomalous data from this crystal at 3.5 Å cutoff and using the refined 2.16 Å Duf8901•Co^{2+} structure (without heteroatoms) as a model. The PHENIX.PHASER run resulted in one substructure solution with two cobalt atoms, with FOM and LLG values of 0.764 and 733.6, respectively, comprising two protomers in the ASU. Phases were optimized by density modification in PHENIX.RESOLVE and used to build initial model in PHENIX.REFINE. The model contained two Duf8901 molecules per ASU and was iteratively improved in PHENIX.REFINE with experimental phase restraints and TLS B-factor refinement (12 TLS groups). NCS restrains were not applied. The final model refined to R_{work}/R_{free} of 20.2/23.5, with 97.4% of the 871 amino acids in the favored regions of the Ramachandran plot and 0.7% outliers.

Duf8901–BeF_3•Ni^{2+} structure

Diffraction data for a single crystal of Duf8901 that had been preincubated with nickel, $BeCl_2$, and NaF were collected at 1.4857 Å wavelength (nickel K-edge) at beamline 24-ID-C. The crystal diffracted to 2.1 Å resolution. Phases were determined by MR-SAD in PHENIX.PHASER by using anomalous data at 3.5 Å cutoff and the Duf8901•Co^{2+} structure (protein without heteroatoms) as a search model. PHENIX.PHASER generated one substructure solution with three nickel atoms and FOM and LLG values of 0.482 and 1980.2. Phases were optimized by density modification in PHENIX.RESOLVE and used to build an initial model in PHENIX.REFINE containing two Duf8901 protomers per ASU. The model was iteratively improved in PHENIX.REFINE with experimental phase restraints and TLS B-factor refinement (11 TLS groups). NCS restraints were not applied. The final Duf8901–BeF_3•Ni^{2+} model refined to R_{work}/R_{free} of 17.9/20.9 with 97.8% of the 872 amino acids in the favored regions of the Ramachandran plot and 0.6% outliers.

Duf8901–BeF_3•Zn^{2+} structure

Diffraction data for a single crystal of Duf8901 that had been preincubated with zinc, $BeCl_2$, and NaF were collected at 1.2822 Å wavelength (zinc K-edge) at beamline 24-ID-C. The crystal diffracted to 2.1 Å resolution. Phases were determined by MR-SAD in PHENIX.PHASER by using anomalous data at 4.3 Å cutoff and the Duf8901•Co^{2+} structure (protein without heteroatoms) as a search model. PHENIX.PHASER generated one substructure solution with two zinc atoms and FOM and LLG values of 0.797 and 1082.6, respectively. Phases were optimized by density modification in PHENIX.RESOLVE and used to build an initial model in PHENIX.REFINE containing two Duf8901 protomers per ASU. The model was iteratively improved in PHENIX.REFINE with experimental phase restraints and TLS B-factor refinement (15 TLS groups). NCS restraints were not applied. The final Duf8901–BeF_3•Zn^{2+} model refined to 17.6/21.6 with 98.3% of the 873 amino acids in the favored regions of the Ramachandran plot and 0.5% outliers.

Duf8901–AlF_4•Co^{2+} structure

Diffraction data from a single crystal of Duf8901 that had been incubated with cobalt, $AlCl_3$ and NaF was collected at 1.6050 Å wavelength (cobalt K-edge) at beamline 24-ID-C. The crystal diffracted to 1.81 Å and belonged to space group I4 with unit cell dimensions consistent with one protomer per ASU, assuming a solvent content of 52%. Initial structure was obtained by MR using Duf8901–BeF_3•Ni^{2+} structure (protein chain A without heteroatoms) as a search model in PHENIX.PHASER suite (TFZ = 69.1; LLG = 5034.2). MR-SAD phases were calculated by combining the MR model from PHASER with anomalous data from this crystal at 2.1 Å resolution cutoff in PHENIX.AUTOSOL (FOM = 0.436). The model contained one Duf8901 molecule per ASU and two cobalt atoms. Phases were optimized by density modification and used in subsequent rounds of iterative refinement in the PHENIX.REFINE suite. Experimental phase restraints and TLS B-factor refinement (11 TLS groups) were applied during refinement. The final model refined to R_{work}/R_{free} of 15.6/18.2, with 98.2% of the 439 amino acids in favored regions of the Ramachandran plot and 0.5% outliers.

Duf89 structure

Diffraction data from a single Duf89 crystal were collected at 1.5895 Å at beamline 24-ID-C. The crystal diffracted to 1.99 Å and belonged to space group C2 with unit cell dimensions consistent with one protomer per ASU, assuming a solvent content of 53%. The Duf89 structure was determined by MR in PHENIX.PHASER using the partially refined 2.75 Å Duf8901 structure (protein only) as a search model. PHENIX.PHASER found 1 MR solution with TFZ and LLG scores of 24.4 and 793.1, respectively, and one Duf89 protomer in the ASU. The 2.0 Å structure was iteratively optimized in PHENIX.REFINE with TLS B-factor refinement (three TLS groups), interspersed with manual building in COOT. The final model refined to R_{work}/R_{free} of 16.0/20.0, with 97.7% of the 440 amino acids in favored regions of the Ramachandran plot and only a single outlier.

Deletion of duf89 *and* duf8901

PCR amplification and standard cloning methods were used to construct plasmids in which the *duf89* gene from nucleotides +5 to +1412 (relative to the translational start codon +1) and the *duf8901* gene from +1 to +1333 were replaced by a *hygMX* and a *kanMX* antibiotic resistance cassette, respectively. The *duf89* and *duf8901* disruption cassettes were excised from the plasmids and transfected into diploid *S. pombe* cells. Hygromycin-resistant and G418-resistant transformants were selected and analyzed by Southern blotting to confirm correct integration at one of the *duf89* loci (thereby deleting amino acids 2–435 of the 442-amino acid Duf89 protein) or one of the *duf8901* loci (deleting amino acids 1–438 of the 438-amino acid Duf8901protein). Hygromycin-resistant *duf89*Δ and G418-resistant *duf8901*Δ

haploids were isolated upon sporulation of the heterozygous diploids. Mating and sporulation of the *duf89*Δ and *duf8901*Δ strains yielded hygromycin/G418-resistant *duf89*Δ *duf8901*Δ double mutants.

Cell-surface acid phosphatase activity

Cells were grown at 30 °C in YES medium. Aliquots of exponentially growing cultures were harvested, washed, and resuspended in water. To quantify acid phosphatase activity, reaction mixtures (200 µl) containing 100 mM sodium acetate (pH 4.2), 10 mM *p*-nitrophenylphosphate, and serial dilutions of cells (ranging from 0.02 to 0.1 at an absorbance at 600 nm units) were incubated for 5 min at 30 °C. The reactions were quenched by addition of 1 ml of 1 M sodium carbonate, the cells were removed by centrifugation, and the absorbance of the supernatant at 410 nm was measured. Acid phosphatase activity is expressed as the ratio of absorbance at 410 nm (*p*-nitrophenol production) to absorbance at 600 nm (cells). The data are averages (±SEM) of at three assays using cells from three independent cultures.

Data availability

The coordinates for the refined models of Duf89, Duf8901•Co^{2+}, Duf8901–BeF_3•Co^{2+}, Duf8901–BeF_3•Ni^{2+}, Duf8901–BeF_3•Zn^{2+}, and Duf8901–AlF_4•Co^{2+} have been deposited in the RCSB protein structure databank under PDB ID codes 7T7N, 7T7K, 7T7O, 7U1V, 7U1X, and 7U1Y. All other data are contained within the article and supporting information.

Supporting information—This article contains supporting information.

Author contributions—A. M. S., A. J., and S. S. conceptualization; A. M. S., A. J., and S. S. investigation; S. S. writing–original draft; A. M. S. and A. J. writing–review and editing; S. S. funding acquisition.

Funding and additional information—This work was supported by the National Institutes of Health grant R35-GM126945 (to S. S.). A. M. S. is supported by the National Science Foundation graduate research fellowship (grant no.: 1746057). The content is solely the responsibility of the authors and does not necessarily represent the official views of the National Institutes of Health. The NE-CAT beamline and the Advanced Photon Source at Argonne National Laboratory are supported by NIH grant P30 GM124165 and Department of Energy Contract No. DE-AC02-06CH11357, respectively.

Conflict of interest—The authors declare that they have no conflicts of interest with the contents of this article.

Abbreviations—The abbreviations used are: AlF_4, aluminum fluoride; ASU, asymmetric unit; BeF_3, beryllium trifluoride; cDNA, complementary DNA; DUF89, Domain of Unknown Function 89; FOM, figure of merit; LLG, log-likelihood gain; lnc, long noncoding; MR, molecular replacement; NCS, noncrystallographic symmetry; SAD, single-wavelength anomalous dispersion; TFZ, translation function Z; TLS, translation libration screw.

References

1. Huang, L., Khusnutdinova, A., Nocek, B., Brown, G., Xu, X., Cui, H., Petit, P., Flick, R., Zallot, R., Balmant, K., Ziemak, M. J., Shanklin, J., de Crecy-Lagard, V., Fiehn, O., Gregory, J. F., *et al.* (2016) A family of metal-dependent phosphatases implicated in metabolite damage-control. *Nat. Chem. Biol.* **12**, 621–627
2. Bitto, E., Bingman, C. A., Allard, S. T., Wesenberg, G. E., and Phillips, G. N. (2005) The structure at 1.7 Å resolution of the protein product of the At2g17340 gene from *Arabidopsis thaliana*. *Acta Crystallogr. Sect. F Struct. Biol. Cryst. Commun.* **61**, 630–635
3. Perry, J. J., Ballard, G. D., Albert, A. E., Dobrolecki, L. E., Malkas, L. H., and Hoelz, D. J. (2015) Human C6orf211 encodes Armt1, a protein carboxyl methyltransferase that targets PCNA and is linked to the DNA damage response. *Cell Rep.* **10**, 1288–1296
4. Dennis, T. N., Kenjic, N., Kang, A. S., Lowenson, J. D., Kirkwood, J. S., Clarke, S. G., and Perry, J. P. (2020) Human ARMT1 structure and substrate specificity indicates that it is a DUF89 family damage-control phosphatase. *J. Struct. Biol.* **212**, 107576
5. Henry, T. C., Power, J. E., Kerwin, C. L., Mohammed, A., Weissman, J. S., Cameron, D. M., and Wykoff, D. D. (2011) Systematic screen of *Schizosaccharomyces pombe* deletion collection uncovers parallel evolution of the phosphate signal transduction pathway in yeasts. *Eukaryot. Cell* **10**, 198–206
6. Shuman, S. (2020) Transcriptional interference at tandem lncRNA and protein-coding genes: An emerging theme in regulation of cellular nutrient homeostasis. *Nucleic Acids Res.* **48**, 8243–8254
7. Sanchez, A. M., Shuman, S., and Schwer, B. (2018) RNA polymerase II CTD interactome with 3' processing and termination factors in fission yeast and its impact on phosphate homeostasis. *Proc. Natl. Acad. Sci. U. S. A.* **115**, E10652–E10661
8. Sanchez, A. M., Garg, A., Shuman, S., and Schwer, B. (2019) Inositol pyrophosphates impact phosphate homeostasis *via* modulation of RNA 3' processing and transcription termination. *Nucleic Acids Res.* **47**, 8452–8469
9. Holm, L., Kaariainen, S., Rosenstrom, P., and Schenkel, A. (2008) Searching protein structure databases with DaliLite v.3. *Bioinformatics* **24**, 2780–2781
10. Cho, H., Wang, W., Kim, R., Yokota, H., Damo, S., Kim, S. H., Wemmer, D., Kustu, S., and Yan, D. (2001) BeF_3^-acts as a phosphate analog in proteins phosphorylated on aspartate: Structure of a BeF_3^- complex with phosphoserine phosphatase. *Proc. Natl. Acad. Sci. U. S. A.* **98**, 8525–8530
11. Kamenski, T., Heilmeier, S., Meinhart, A., and Cramer, P. (2004) Structure and mechanism of RNA polymerase II CTD phosphatases. *Mol. Cell* **15**, 399–407
12. Ghosh, A., Shuman, S., and Lima, C. D. (2008) The structure of Fcp1, and essential RNA polymerase II CTD phosphatase. *Mol. Cell* **32**, 478–490
13. Miao, Y., Tenor, J. L., Toffaletti, D. L., Washington, E. J., Liu, J., Sadrick, W. R., Schumacher, M. A., Lee, R. E., Perfect, J. R., and Brennan, R. G. (2016) Structures of trehalose-6-phosphate phosphatase from pathogenic fungi reveal the mechanisms of substrate recognition and catalysis. *Proc. Natl. Acad. Sci. U. S. A.* **113**, 7148–7153
14. Baxter, N. J., Blackburn, G. M., Marston, J. P., Hounslow, A. M., Cliff, M. J., Bermel, W., Williams, N. H., Hollfelder, F., Wemmer, D. E., and Waltho, J. P. (2008) Anionic charge is prioritized over geometry in aluminum and magnesium fluoride transition state analogs of phosphoryl transfer enzymes. *JACS* **130**, 3952–3958
15. Guhaniyogi, J., Robinson, V. L., and Stock, A. M. (2006) Crystal structures of beryllium fluoride-free and beryllium fluoride-bound CheY in complex with the conserved-terminal peptide of CheZ reveal dual binding modes specific to CheY conformation. *J. Mol. Biol.* **359**, 624–645
16. Schwer, B., Garg, A., Sanchez, A. M., Bernstein, M. A., Benjamin, B., and Shuman, S. (2022) Cleavage-polyadenylation factor Cft1 and SPX domain proteins are agents of inositol pyrophosphate toxicosis in fission yeast. *mBio* **13**, e0347621
17. Fankhauser, H., Zurlinden, A., Schweingruber, A. M., Edenharter, E., and Schweingruber, M. E. (1995) *Schizosaccharomyces pombe* thiamine

pyrophosphokinase is encoded by gene tnr3 and is a regulator of thiamine metabolism, phosphate metabolism, mating, and growth. *J. Biol. Chem.* **270**, 28457–28462
18. Nahas, J. V., Iosue, C. L., Shaik, N. F., Selhorst, K., He, B. Z., and Wykoff, D. D. (2018) Dynamic changes in yeast phosphatase families allow for specialization in phosphate and thiamine starvation. *G3 (Bethesda)* **8**, 2333–2343
19. Kabsch, W. (2010) Xds. *Acta Crystallogr. D Biol. Crystallogr.* **66**, 125–132
20. Evans, P. R., and Murshudov, G. N. (2013) How good are my data and what is the resolution? *Acta Crystallogr. D Biol. Crystallogr.* **69**, 1204–1214
21. Adams, P. D., Afonine, P. V., Bunkóczi, G., Chen, V. B., Davis, I. W., Echols, N., Headd, J. J., Hung, L. W., Kapral, G. J., Grosse-Kunstleve, R. W., McCoy, A. J., Moriarty, N. W., Oeffner, R., Read, R. J., Richardson, D. C., *et al*. (2010) PHENIX: A comprehensive Python-based system for macromolecular structure solution. *Acta Crystallogr. D Biol. Crystallogr.* **66**, 213–221
22. Emsley, P., and Cowtan, K. (2004) Coot: Model-building tools for molecular graphics. *Acta Crystallogr. D Biol. Crystallogr.* **60**, 2126–2132
23. Kelley, L. A., Mezulis, S., Yates, C. M., Wass, M. N., and Sternberg, J. E. (2015) The Phyre2 web portal for protein modeling, prediction and analysis. *Nat. Protoc.* **10**, 845–858